



## RESEARCH ARTICLE

10.1029/2021JF006256

# Rock Glacier Characteristics Under Semiarid Climate Conditions in the Western Nyainqêntanglha Range, Tibetan Plateau

## Key Points:

- Geophysical and remote sensing methods in concert reveal the morphostructure, ice fraction, and kinematics of the studied rock glacier
- Rock glacier characteristics are controlled by geology, topography and climate on the Tibetan Plateau
- The studied rock glacier is conceptually interpreted as the endmember of a glacier—debris-covered glacier—rock glacier continuum

## Supporting Information:

Supporting Information may be found in the online version of this article.

## Correspondence to:

J. Buckel,  
[j.buckel@tu-braunschweig.de](mailto:j.buckel@tu-braunschweig.de)

## Citation:

Buckel, J., Reinosch, E., Voigtländer, A., Dietze, M., Bucker, M., Krebs, N., et al. (2022). Rock glacier characteristics under semiarid climate conditions in the western Nyainqêntanglha range, Tibetan Plateau. *Journal of Geophysical Research: Earth Surface*, 127, e2021JF006256. <https://doi.org/10.1029/2021JF006256>

Received 10 MAY 2021  
Accepted 20 DEC 2021

Johannes Buckel<sup>1</sup> , Eike Reinosch<sup>2</sup>, Anne Voigtländer<sup>3</sup> , Michael Dietze<sup>3</sup> , Matthias Bucker<sup>1</sup>, Nora Krebs<sup>4</sup>, Ruben Schroeckh<sup>5</sup>, Roland Mäusbacher<sup>6</sup>, and Andreas Hördt<sup>1</sup>

<sup>1</sup>Institute for Geophysics and Extraterrestrial Physics, Technische Universität Braunschweig, Braunschweig, Germany,

<sup>2</sup>Institute for Geodesy and Photogrammetry, Technische Universität Braunschweig, Braunschweig, Germany, <sup>3</sup>GFZ

German Research Centre for Geosciences, Potsdam, Germany, <sup>4</sup>World Meteorological Organization, Geneva, Switzerland,

<sup>5</sup>Department of Geography and Geology, University of Salzburg, Salzburg, Austria, <sup>6</sup>Geographical Institute, Friedrich Schiller University of Jena, Jena, Germany

**Abstract** Rock glaciers are receiving increased attention as a potential source of water and indicator of climate change in periglacial landscapes. They consist of an ice-debris mixture, which creeps downslope. Although rock glaciers are a wide-spread feature on the Tibetan Plateau, characteristics such as its ice fraction are unknown as a superficial debris layer inhibits remote assessments. We investigate one rock glacier in the semiarid western Nyainqêntanglha range (WNR) with a multi-method approach, which combines geophysical, geological and geomorphological field investigations with remote sensing techniques. Long-term kinematics of the rock glacier are detected by 4-year InSAR time series analysis. The ice content and the active layer are examined by electrical resistivity tomography, ground penetrating radar, and environmental seismology. Short-term activity (11-days) is captured by a seismic network. Clast analysis shows a sorting of the rock glacier's debris. The rock glacier has three zones, which are defined by the following characteristics: (a) Two predominant lithology types are preserved separately in the superficial debris patterns, (b) heterogeneous kinematics and seismic activity, and (c) distinct ice fractions. Conceptually, the studied rock glacier is discussed as an endmember of the glacier—debris-covered glacier—rock glacier continuum. This, in turn, can be linked to its location on the semiarid lee-side of the mountain range against the Indian summer monsoon. Geologically preconditioned and glacially overprinted, the studied rock glacier is suggested to be a recurring example for similar rock glaciers in the WNR. This study highlights how geology, topography and climate influence rock glacier characteristics and development.

**Plain Language Summary** Climate change has begun to impact all regions of our planet. In cold regions, such as high-mountain areas, rising temperatures lead to massive melting of glaciers. Besides this evident loss of ice, permafrost, a long-term ice resource hidden in the subsurface, has started to thaw. Rock glaciers as visible permafrost-related landforms consist of an ice-debris mixture, which makes them creep downslope. Due to this movement and their recognizable shape, rock glaciers are permafrost indicators in high-mountain areas. We investigate one rock glacier in the western Nyainqêntanglha Range (Tibetan Plateau) using field and remote sensing methods to understand its development and to know the current state of its ice core. Our main outcome is, that the heterogeneous creeping behavior, the properties of the debris cover as well as the internal distribution of ice are the results of a continuous development from a glacier into today's rock glacier. In particular, the high ice content in particular sections points to such a glacial precondition. The debris layer covering the internal ice attenuates the effect of climate warming. This makes the rock glacier and similar rock glaciers found in the northern part of the mountain range important future water resources for the semiarid region.

## 1. Introduction

In the context of climate change, glacial and periglacial landscapes are receiving increased attention as a water resource, especially in semiarid climates with growing population, for example, the Tibetan Plateau (Bolch et al., 2019; Hock et al., 2019; Immerzeel et al., 2020; Sun et al., 2018). Glacial and periglacial landforms are sensitive to climate warming and represent significant water reservoirs in semiarid environments and lowlands

© 2022. The Authors.

This is an open access article under the terms of the [Creative Commons Attribution License](https://creativecommons.org/licenses/by/4.0/), which permits use, distribution and reproduction in any medium, provided the original work is properly cited.

(Halla et al., 2021; Jones, Harrison, Anderson, & Betts, 2018; Jones, Harrison, Anderson, Selley, et al., 2018; Karjalainen et al., 2020; Kellerer-Pirklbauer et al., 2017; Müller et al., 2016). In the western Nyainqêntanglha range on the Tibetan Plateau periglacial conditions and related landforms prevail (Anslan et al., 2020; Buckel et al., 2021; Keil et al., 2010; Reinosch et al., 2020). Periglacial landforms are generally made of a mix of ice, rock debris and sediment (French, 2017; Haeberli et al., 2006). Visible features include rock glaciers, which are primarily comprised of angular-rock debris and interstitial ice, ice lenses, and a coarse outer debris layer, which freezes and thaws seasonally. This so-called active layer provides insulating and damping properties against atmospheric influences (Barsch, 1996; Haeberli et al., 2006) and suggests that rock glaciers are climatically more resistant than debris-free and debris-covered glaciers (Jones et al., 2021). Thus, rock glaciers are expected to have a long-term importance for water supply under the current global warming trend (Halla et al., 2021; Jones, Harrison, Anderson, & Whalley, 2019; Juliussen & Humlum, 2008; Millar et al., 2013).

Gravity-driven creep of debris and interstitial ice are key signs of an active rock glacier (Barsch, 1996; French, 2017; Haeberli et al., 2006). The movement creates a lobate or tongue shaped landform with typical furrows and ridges (Janke & Frauenfelder, 2008). The lithologic composition and the resulting clast size of rock glaciers is indicative of its kinematics, activity and ice content (Barsch, 1996; Degenhardt, 2009; Kellerer-Pirklbauer et al., 2017). Although a widespread feature on the Tibetan Plateau (Buckel & Reinosch, 2021; Z. Ran & Liu, 2018; Reinosch et al., 2021), rock glacier characteristics and water storage potential have not been investigated in great detail.

Due to their high elevation and remote location, rock glaciers are usually assessed with remote sensing techniques (Jones et al., 2021; Z. Ran & Liu, 2018; Reinosch et al., 2021; Schmid et al., 2015; Villarroel et al., 2018). Interferometric Synthetic Aperture Radar (InSAR) is widely used to study surface displacements of rock glaciers and their variations over several years (Berardino et al., 2002). A recent study in the western Nyainqêntanglha range also identifies the active status of rock glaciers by surface displacement rates obtained from perennial InSAR data (Reinosch et al., 2021). Although these studies are able to characterize the spatial distribution and activity of rock glaciers, there is a general lack of ground truth data, and direct information on subsurface ice fraction at the Tibetan Plateau. This information is crucial for a discussion and understanding of the role of rock glaciers in the context of climate warming and water storage capacities. To assess the internal structure of a rock glacier, several geophysical methods should be applied in combination with geomorphological and geological assessments of the surrounding headwalls and rock materials (Farbrot et al., 2005; Ikeda, 2006; Kellerer-Pirklbauer & Kaufmann, 2018; Maurer & Hauck, 2007; Winsor et al., 2020). A recent study employed environmental seismology to assess spatial and short-term activity patterns of a single rock glacier (Guillemot et al., 2020). However, studies about detailed characterization of rock glaciers (e.g., Blöthe et al., 2020; Halla et al., 2021; Hausmann et al., 2007; Kellerer-Pirklbauer & Kaufmann, 2018; Kellerer-Pirklbauer et al., 2017; Maurer & Hauck, 2007; Müller et al., 2016) are lacking at the Tibetan Plateau.

Generally, the characteristics and development of rock glaciers are driven by lithology (e.g., Ikeda & Matsuoka, 2006; Matsuoka & Ikeda, 2001) and climate conditions (e.g., Monnier & Kinnard, 2017; Washburn, 1980) and are therefore controlled by the availability of water, ice and also, rock debris (Barsch, 1996; Knight et al., 2019). In addition to the initial setting controlling rock glacier formation (Bolch & Gorbunov, 2014; Kellerer-Pirklbauer & Kaufmann, 2018; Winsor et al., 2020), concepts of its evolution pathways have also been proposed: Anderson et al. (2018) modeled a continuous pathway by using different states of the equilibrium line altitude (ELA) to describe the evolution of a glacier into a debris covered glacier and finally into a rock glacier as an endmember. The increase of debris amount in this continuum delayed the response of the debris-covered glaciers of melting to climate warming (Collier et al., 2015) and its evolution into the endmember “rock glacier” (Anderson et al., 2018). The internal ice fraction is therefore a significant and persistent fresh water resource considering that glaciers without debris cover usually melt during an early stage of climate warming (Azócar & Brenning, 2010; Jones et al., 2021; Jones, Harrison, Anderson, & Betts, 2018; Monnier & Kinnard, 2015). Knight (2019) and Knight et al. (2019) identify the mutual dependencies between three factors “water-sediment-temperature” wherein the dominant (glacial-periglacial-paraglacial) processes lead to a specific evolutionary rock glacier type. Monnier and Kinnard (2017) highlighted the interaction between glacially and periglacially driven landform evolutions and suggested a non-continuous pathway in the glacier to rock glacier transition. These concepts overcome a unilateral explanation (glacial or periglacial) of rockglacier development including the coexistence of different rock glacier evolution types.

In semiarid and highly elevated mountain ranges, like the northern part of the western Nyainqêntanglha range (Anslan et al., 2020; Bolch et al., 2010), the extent of the source areas for moisture and sediment of the rock glacier might be limited (Blöthe et al., 2020; Humlum, 2000; Janke & Frauenfelder, 2008). In general, the moisture of rock glacier ice can originate from precipitation, snow or glacial melt, as well as debris-covered glacial remnants. To allow water and moisture to intersperse and refreeze inside a rock glacier, a sufficient sediment amount and size need to be available (Jones, Harrison, & Anderson, 2019; Rowley et al., 2015). For example, ice can aggregate more easily in smaller grain size due to the high capillary pressure and water retention potential (French, 2017). Due to reduced moisture availability in semiarid climates chemical weathering is limited (Yu et al., 2019). Therefore, the availability of greater sized sediments and a general lack of moisture might be the main limiting factors for distinctive periglacial ice aggregation.

We characterize one single rock glacier with respect to the morphostructure (geomorphic and geologic characterization), the internal ice distribution as well as the kinematics using a suite of field and remote sensing methods. Additionally, the studied rock glacier is located in a special climate setting (intersection of the Indian summer monsoon and the Westerlies), which characterizes the northern part of the western Nyainqêntanglha range as a semiarid region (Anslan et al., 2020).

By investigating this rock glacier, we aim at better understanding its characteristics with respect to: (a) internal structure (debris and ice distribution), (b) current state as well as dynamics, and (c) the local conditions, which control the location and formation of the rock glacier within the semiarid environment of the western Nyainqêntanglha range and which are indicated by a regionalization using the studied rock glacier as an endmember in a recurrent toposequence. To achieve this, we use a complementary approach which combines remote sensing, geophysical, geomorphological and geological methods.

## 2. Study Area

The Nyainqêntanglha range, with elevations up to 7,162 m a.s.l., on top of the Tibetan Plateau (~3,500–4,500 m a.s.l.) poses a NE-SW oriented topographic barrier to the two dominating and seasonal wind systems, the Indian Summer Monsoon (ISM) from the south and the Westerlies (T. Yao et al., 2013; Yatagai & Yasunari, 1998) (Figures 1a and 1b). The barrier creates a climatic and hydrological divide between the semiarid catchment of the lake Nam Co (300 mm/y) in the North and the Yangbajain-Damxung valley (460 mm/yr) as part of the Tsangpo-Brahmaputra River system in the South of the mountain range (Anslan et al., 2020; Keil et al., 2010). Due to the difference in moisture availability, a more extensive glaciation (Bolch et al., 2010) and greater numbers of rock glaciers have been observed in the Southern (1133) than in the Northern part (300) of the Nyainqêntanglha Range shown by a rock glacier inventory (Buckel et al., 2021; Reinosch et al., 2021). 91.3% of the active rock glaciers are located in the Southern part of the water divide. Rock glaciers cover an area of 124.9 km<sup>2</sup> at the mountain range while the glaciated area covers 575.7 km<sup>2</sup> (Reinosch et al., 2021). G. Li and Lin (2017) identify a glacial mean annual mass loss rate of 0.127 m w.e./yr for the entire range.

The investigated rock glacier is max. 750 m long, max. 430 m wide and covers an area of 0.24 km<sup>2</sup> in the Qugaqie basin (Figures 1b and 1c). It ranges from 5,466 to 5,566 m a.s.l. and shows an overall tongue shape. It is located within a glacial cirque orientated towards NNE, where the slopes are interrupted by a flat valley plain in between. Since the rock glacier rests within a narrow valley, all adjacent slopes can potentially contribute debris, sediment, and water toward it. Directly adjacent to the north-orientated landform a cirque glacier covers the leeward (in ISM direction) valley head (Figures 1c and 2, location map). This cirque glacier is free of superficial debris and seems disconnected from the valley plain. The rock glacier's headwall is more than 35° steep and periodic sediment release was audible and visible during field work 2019 (8–22 November 2019) due to high rock fall activity.

The semiarid conditions are further enhanced by the high evapotranspiration rates due to high atmospheric transmissivity for solar radiation and a generally low cloud cover at these high elevations (Duan et al., 2012; J. Li et al., 2009; Wang et al., 2019). The mean annual air temperatures for the Nyainqêntanglha Range are generally below 0°C leading to the presence of permafrost (Keil et al., 2010; B. Li et al., 2014). It is assumed that 40%–60% of the mountains contain permanently frozen ground (Zou et al., 2017), classified as high-altitude isolated permafrost (Y. Ran et al., 2012). Since the quaternary glaciations, the highest peaks of the Nyainqêntanglha range have been continuously glaciated (Bolch et al., 2010). Prominent moraine ridges suggest a former valley floor glaciation at the northern part of the mountain range (Buckel et al., 2021; Dong et al., 2014). Above the lateral

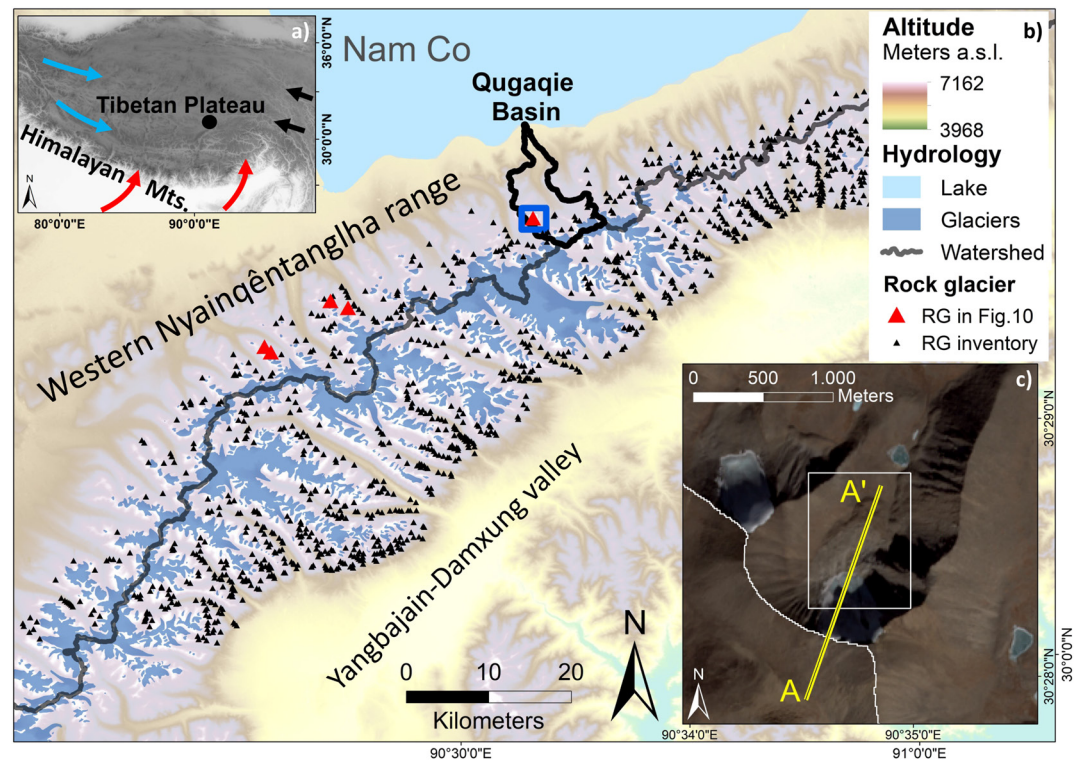


**Figure 1.** Location of the study area. (a) Location (black dot) of the western Nyainqêntanglha range at the Tibetan Plateau (elevation data based on SRTM DEM v4; Jarvis et al., 2008) and the dominant wind systems: westerlies (blue arrows), Indian summer monsoon (red arrows), and East Asian monsoon (black arrows) based on T. Yao et al. (2012). (b) Overview map of the western Nyainqêntanglha range and the Qugaqie basin (thick black lines). Glacier extents originated from GLIMS database (Cogley et al., 2015; Guo et al., 2015). The blue rectangle locates the optical image of map (c). (c) Southern part of the Qugaqie basin including the studied rock glacier (white rectangle, shown in Figure 2). The yellow line indicates the location of the profile of panel (a) in Figure 10. Background based on Sentinel II satellite image, recorded 30 January 2018.

moraines, south-orientated debris mantled slopes dominate the valleys of the northern part of the western Nyainqêntanglha range (Fort & van Vliet-Lanoe, 2007).

The general geological makeup of the Nyainqêntanglha range is based on Cretaceous to Tertiary Granitoids and Orthogneiss (Edwards and Ratschbacher, 2005; Kidd et al., 1988; Law & Allen, 2020). Following the National Geological Archives of China (NGAC), the dominant lithology in the studied catchment is granodiorite (Yu et al., 2019). Two major fault systems dissect the Nyainqêntanglha massive in this area. Normal faults with a NE-SW strike, parallel to the orientation of the mountain range, have been associated with the orthogenesis of the Tibetan Plateau (Armijo et al., 1986; Blisniuk et al., 2001; England & Houseman, 1989; Molnar & Tapponnier, 1978; Taylor et al., 2003; Yin & Harrison, 2000; Yin et al., 1999) and SE dipping normal detachment faults which transition at depth into low-angle shear zones (Harrison et al., 1992; Kapp et al., 2005).

### 3. Materials and Methods

To characterize the rock glaciers interior, morphology and surrounding we followed an approach two, but nested, spatial scales. At the local scale, the applied methods can be further divided into short and long-term investigations. The local short-term methods resemble geophysical, geological and geomorphic field measurements. Geophysical field methods, like electrical resistivity tomography (ERT) and ground penetration radar (GPR) are employed to detect the fraction of ice and debris in the composition of the rock glacier. Local mapping and investigations of lithology and morphology of the rock glacier and its surrounding catchment are complimented by remote sensing. To assess short-term kinematical dynamics and possible temporal variations (from hours to days), we use a small seismic network on the rock glacier. For the longer-term (here four years) surface displacement rates and kinematics of the rock glacier we use InSAR-data. All methods are introduced in detail in

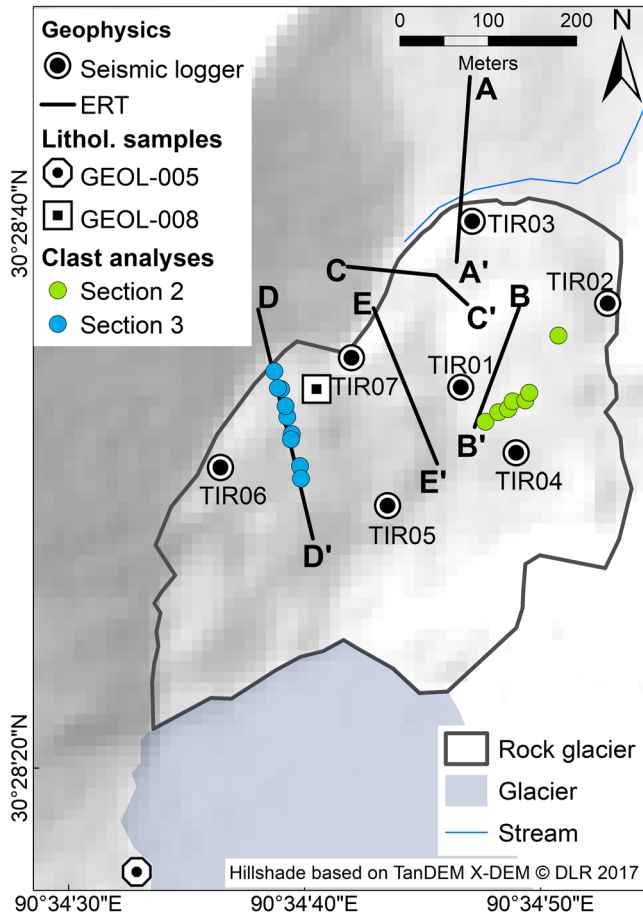


**Figure 2.** Location of the applied field methods. Note that the ground penetration radar profile was collected along the electrical resistivity tomography tomogram D. The map encompasses the area marked by the white rectangle in Figure 1c.

the following subsections. The location of the used geophysical methods, the sample locations and the location of the clast analyses are given by the map in Figure 2. The found characteristics suggest a zonation of the rock glacier in three parts. This zonation is recurrent in the findings of each applied method and is used to interpret the data. In an attempt to extrapolate our findings to the regional scale, the western Nyainqêntanglha range, we use a conceptual approach (Anderson et al., 2018) combined with an existing rock glacier inventory (Figure 1b, Buckel & Reinosch, 2021). We aim to identify similar topographic profiles with similar rock glaciers as endmembers, so called “toposequences.”

### 3.1. Morphostructure and Geology

We use structural geological and geomorphological mapping techniques in the field as well as remote analysis of a digital elevation model (DEM) to characterize the catchment and the morphostructure of the rock glacier. We mapped ridge and furrow distribution in the field and remotely. For the ridge mapping, the location and the extent of ridges were tracked in the field by a handheld global positioning system (GPS) device with a precision of approximately 6 m depending on the availability of satellites. Geological structures and distributions were mapped in the field.

To assess surface debris sizes, shapes and orientations, we measured the dimensions of clasts using a modified pebble count approach (after Ballantyne, 1982). The method has been developed to quantify debris size distributions in fluvial transport (Wolman, 1954), but has also been applied in glacier and rock glacier studies to track the debris origin and to evaluate erosional, transportational and depositional processes (Benn & Ballantyne, 1993, 1994; Lukas et al., 2013; Sampson & Smith, 2006). Along two transects of about 150 m length covering furrows and ridges, perpendicular to the rock glacier ridges surface slope, we sampled size and shape of clasts at 16 samplings sites. Each sampling site was a 2 m long scan line. Along this scan line, clasts larger than 1 cm were considered in the analysis. We modified the method so far as that we measure parallel and perpendicular to the scan line (meaning: a—line parallel; b—line perpendicular and horizontal; c—line perpendicular and vertical). In this way the ratio between the  $x$  and  $y$  axis gives estimation

for the orientation of the surface clast relative to the scan line. A total of 428 clasts have been measured by this way.

For the lithological identification of the debris source areas, we used a geological map (Yu et al., 2019), and collected rock samples and analyzed them with a hand held lens in field as well as by thin sectioning (25  $\mu$ m thickness) in the laboratory.

### 3.2. Geophysical Methods

Geophysical methods provide information about the subsurface non-invasively. Inhomogeneities and internal structures of the subsurface are displayed based on physical properties (conductivity, permittivity, etc.) of various materials. We used three geophysical methods (Sections 3.2.1–3.2.3) to derive the active layer and to differentiate information about the debris and the subsurface ice fraction.

#### 3.2.1. ERT

ERT provides two-dimensional tomograms of the subsurface electrical resistivity, that is, the variation of the resistivity in the horizontal and vertical direction. The electrical resistivity of ice is particularly high compared to that of other materials. Therefore, ERT is a useful tool to identify subsurface ice distribution in cryospheric research. We measured five ERT profiles (Figure 2; profiles a–e) with the Wenner array-type during two field

seasons in July 2018 and September 2019. The aim of the first field season was to assess the occurrence of subsurface ice. In this context, the three tomograms (b–d) (spacing 2 m) have already been discussed by Buckel et al. (2021). During the second field season, two additional tomograms (a and e) were acquired with a larger spacing of 4 m to further investigate the internal structure of the rock glacier and to assess the subsurface ice distribution down to greater depths. Tomograms (b–d) are used in this study to characterize different subsurface ice distributions. Profile A covers the frontal lobe of the rock glacier to deduce ice content and the status of activity. The profile crosses a stream originating from the rock glacier spring.

The data acquisition was carried out with the “GeoTom-MK” (GEOLOG2000, Augsburg, Germany) equipped with 75 electrodes, partly by the roll-along procedure (Buckel et al., 2021). Steel pikes placed in wet sponges and fine grained material reduced the usually high coupling resistance on the blocky rock-glacier surface. Data inversion was performed using the Res2Dinv software (©Geotomo Software), which uses a smoothness-constraint least squares inversion approach (Loke & Barker, 1995) to adjust a subsurface resistivity model to the measured data. Topographic information was included in both the inversion process and the final visualization of the profiles. Further details on field procedure and inversion are given in Buckel et al. (2021).

In order to obtain subsurface ice distribution from the ERT tomograms, we classify the substrate into four types depending on the resistivity: unfrozen substrate ( $<50$  k $\Omega$ m), ice-poor permafrost (50–150 k $\Omega$ m), ice-rich permafrost (150–2,000 k $\Omega$ m) and substrate-poor ice ( $>2,000$  k $\Omega$ m). Our classification is based on resistivity values of different rock glaciers in the Alps (Hauck & Kneisel, 2008; Kneisel et al., 2008; Mewes et al., 2017; Von der Mühl et al., 2002).

The main challenges and uncertainties in the method in this terrain arise from the coupling of the pikes to the substrate to allow current flow (Hauck & Kneisel, 2008; Krebs et al., 2020). Finer substrate which is usually used to stick the pikes into the ground, is absent on the rough and blocky surface of a rock glacier. Sponges and salted water can improve the coupling of the pike electrodes to the blocks in direct contact (Hauck & Kneisel, 2008). However, if the contact to the underlying blocks is poor due to lack of fine substrate, no sufficient current can be injected and/or voltage readings become unstable. In either case, measurements carried out with the corresponding electrode are not suitable for assessing the subsurface resistivity. In such cases, we shifted the pikes to locations which provided better coupling conditions but were also as close as possible (max. 1 m) to the original position.

### 3.2.2. GPR

In addition to ERT, GPR can provide information on the inner structure of a rock glacier, in particular, the active layer thickness and ice-debris composition. In order to cross validate the interpretation of the ERT tomogram, common-offset GPR data was collected using a Noggin® GPR system (Sensors and Software, Ontario, Canada) with a 100 MHz antenna along the first 253 m of profile (d) (Figure 2). Measurements were triggered manually with a unit spacing of 1 m. The shortening of the GPR profile by 25 m (in comparison to the ERT profile d) was due to the risk of injury from large unstable blocks along the last part of the profile. Processing of the GPR data included: (a) high-pass filtering of single-trace data with a cut-off frequency of  $\sim 60$  MHz (instead of Dewow filtering), (b) subtraction of the average signal (computed as the moving average over 100 neighboring traces) for background removal, (c) low-pass filtering of single-trace data with a cut-off frequency of 200 MHz to remove high-frequency noise, and (d) application of time-dependent gains based on an exponential compensation approach. The processing steps were implemented in MATLAB (Supporting Information S1). We used an estimated wave velocity of  $v \approx 0.134$  m ns $^{-1}$  (i.e., relative permittivity  $\epsilon_r = 5$ ), which is an average value for frozen to unfrozen ground (e.g., Otto et al., 2012), to convert two-way travel times into a depth scale for the GPR profile. Topographic information was included in the final visualization of the radargram. For detailed information, please refer to Supporting Information S1.

Uncertainties result from errors in timing, wave-velocity estimate, and the horizontal location along the profile for a quantitative analyze of the GPR data (Lapazaran et al., 2016). As we interpret GPR data qualitatively, such errors only play a secondary role. Instead, we consider the orientation of the antenna on the rough surface of the rock glacier the main source of error: The blocky material and the varying orientation of the surfaces of the individual blocks result in antenna orientations, which may not be parallel to the topography. This uncertainty in the antenna orientation results in an error in the location of GPR reflections, especially at larger depths. However, as

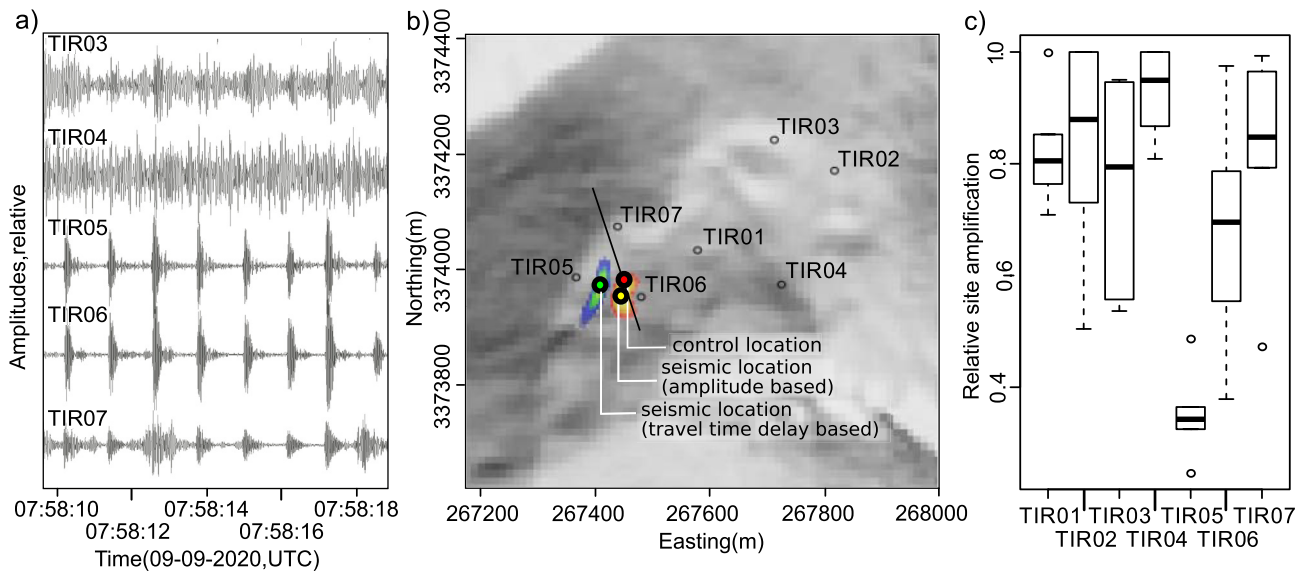


**Figure 3.** Illustration of the calibration procedure. (a) Seismograms of control events (filtered between 20 and 40 Hz). (b) Map of the control event location (red circle) and results of seismic approaches with optimized parameters (i.e., apparent wave velocity = 1,600 m/s, ground quality factor = 80). The black line indicates Profile D in Figure 2. (c) Site amplification factors for all seismic stations as obtained by averaging results of six regional earthquakes.

the GPR profile is much longer (253 m) than deep (~20 m), this error does not significantly affect our qualitative interpretation with regard to the zonation of the rock glacier.

### 3.2.3. Seismic Monitoring (Short-Term Kinematics)

To study the expressions of short-term kinematics of the landform, we installed a small network of seven seismic stations (geophones) on the rock glacier (Figure 2). Data collected over an 11 day period from 10 September 2019 to 21 October 2019 were analyzed with the software “eseis v. 0.6.0” (Dietze, 2018a, 2018b). The analysis focused on three objectives: (a) determining the active layer thickness by passive seismic noise analysis, (b) detecting and locating seismic signals due to cracks emerging from the landform under investigation (see Text S2 in Supporting Information S1 for details), and (c) by complementing InSAR’s low sensitivity toward northward and southward displacement.

The lower boundary of the active layer of rock glaciers usually exhibits a strong contrast in seismic wave velocity (Guillemot et al., 2020). Thus, horizontal to vertical spectral ratio (HVSr) analysis (Del Gaudio et al., 2014; Nogoshi & Igarashi, 1971) can provide a convenient way to estimate the thickness of the active layer in the vicinity of the station, assuming a constant underground structure with a well-defined active layer boundary as well as a homogeneous distributed seismic wave source. Hence, either weak velocity contrasts or spatially changing active layer thicknesses, or local amplifications of seismic noise sources can lead to poorly defined HVSr results. In contrast, stable resonance peaks of the HVSrs, calculated from 10 min long time snippets, relate to layer thickness through the shear wave velocity, which we estimated to be 325–426 m/s (Guillemot et al., 2020). For the second objective, the seismic data was automatically screened with a classic event detection routine (STA-LTA-ratio picker; Allen, 1982) and false events were rejected based on expected minimum and maximum crack signal durations, frequency content and lacking co-detection by multiple stations (Polvi et al., 2020; Weber et al., 2018). The remaining crack signals were located using the amplitude modeling technique (Walter et al., 2017) and the resulting event locations were regionalized with a 2D kernel density interpolator (Baddeley et al., 2015). The temporal occurrence of events was analyzed at the diurnal scale and throughout the 11 days survey period. For detailed information, we refer to Supporting Information S1.

Parameters that were essential for the crack signal location approach have been constrained by measuring the time differences between waveforms at station pairs with known distances to control sources. For the control sources, we used field activities at known locations. As an example, the data for hammer blows to deploy ERT probes are shown in Figures 3a and 3b. Seismic location estimates of these regular signals (Figure 3a) were closest to the known origins (Figure 3b) when using an apparent seismic wave velocity of 1,600 m/s for the signal migration

approach (used here only to constrain the velocity estimate, for details on the method see Dietze et al. [2020]), and a ground quality factor of 80. Both approaches yield the correct location with a deviation of less than 20 m, that is, about 7% of the average station spacing, a value in the range of other studies (Dietze, 2018a, 2018b; Polvi et al., 2020).

### 3.3. InSAR-Time Series Analyses

The InSAR technique is frequently used to monitor earth's surface displacements with remote sensing methods. It has been used in numerous recent studies to assess the surface velocity of rock glaciers in the Andes, the European Alps, the Tien Shan, and the Tibetan Plateau (Kääb, 2008; Reinosch et al., 2021; Strozzi et al., 2020).

Here, we use InSAR-data of the Sentinel-1 satellite to detect the long-term kinematics of the rock glacier. The surface displacement calculated here is one-dimensional and provides information only along the line-of-sight (LOS) of the satellite, meaning that only displacement toward the satellite or away from it can be observed. The LOS of the Sentinel-1 satellite results in a high sensitivity to vertical displacements and to displacements toward the east or west. Its sensitivity to displacement toward the north or south is therefore low (Reinosch et al., 2020). We use acquisitions of both the ascending and the descending orbit (i.e., when the satellite is traveling south to north and north to south, respectively). We refer the reader to Reinosch et al. (2020) for a more detailed description of data and processing. Sentinel-1 acquisitions of our study area are available at mostly 24–48 days intervals in 2015 to 2016 and at 12-day intervals from 2017 onwards. We use 74 ascending acquisitions and 63 descending acquisitions from 2015 to 2018.

We apply the Small Baseline Subset (SBAS) technique (Berardino et al., 2002), which uses multiple consecutive InSAR pairs to estimate the surface displacement of the area of interest over a period of several months to years. Intermittent SBAS (adapted by Sowter et al. [2013]) allows the interpolation of time periods where the coherence of a pixel drops below a chosen threshold. We chose a coherence threshold of 0.3 which a pixel needs to exceed during at least 75% of the observation time. This value is similar to the one used by Sowter et al. (2013) and achieves high spatial coverage without including areas with high signal-to-noise ratios such as wetlands or glaciers. Spatial data gaps indicate areas where the coherence is below our chosen threshold of 0.3 for more than 25% of the observation period. Low coherence values are caused by changing backscatter properties (e.g., from snow cover), different motion directions within one resolution cell or sudden displacements, like rock falls.

The motion of rock glaciers is generally gravity-driven and directed downslope (Barsch, 1996). We therefore projected the LOS displacement onto the direction of the steepest slope following the method described by Notti et al. (2014). The precision of the projected surface velocity was estimated to vary from 2 to 12 mm/yr depending on the displacement direction (Buckel et al., 2021). Grebby et al. (2019) calculated a root-mean-square-error of 3.18 mm/yr when comparing their LOS SBAS results to leveling data near oil fields in Kazakhstan. No in situ data is available for our study area, making an accurate assessment of the precision of the velocity data rather difficult. On likely stable moraines we observe a standard deviation of 2.4 mm/yr in LOS. This would equate to a standard error of 2.4–12.0 mm/yr for the projected surface velocity depending on the displacement direction (Buckel et al., 2021). The velocity of approximately northward or southward creeping areas is greatly underestimated by InSAR techniques. To compensate for the underestimation, a larger projection coefficient is used when projecting the LOS velocity in the direction of the steepest slope in these areas, thereby also leading to a larger standard error. This directional sensitivity of InSAR for the estimation of surface displacements is a methodological drawback which may be compensated by the comparison with independent data, such as environmental seismology.

## 4. Results

### 4.1. Morphostructure

The rock glacier, situated in a glacial cirque, shows a tongue shape form and is max. 750 m long, max. 430 m wide. A heterogeneity in terms of its ridge location is observed (Figure 4): There are two major ridges and seven minor ridges. Section 1 represents the frontal part of the rock glacier, characterized by a single ridge on top of the lobe. The slope of the lobal front reaches a maximum angle of 30°. A long ridge dominates the eastern part (Section 2) of the rock glacier. As indicated by the small slope angle and the contours (around 5,490 m a.s.l.),

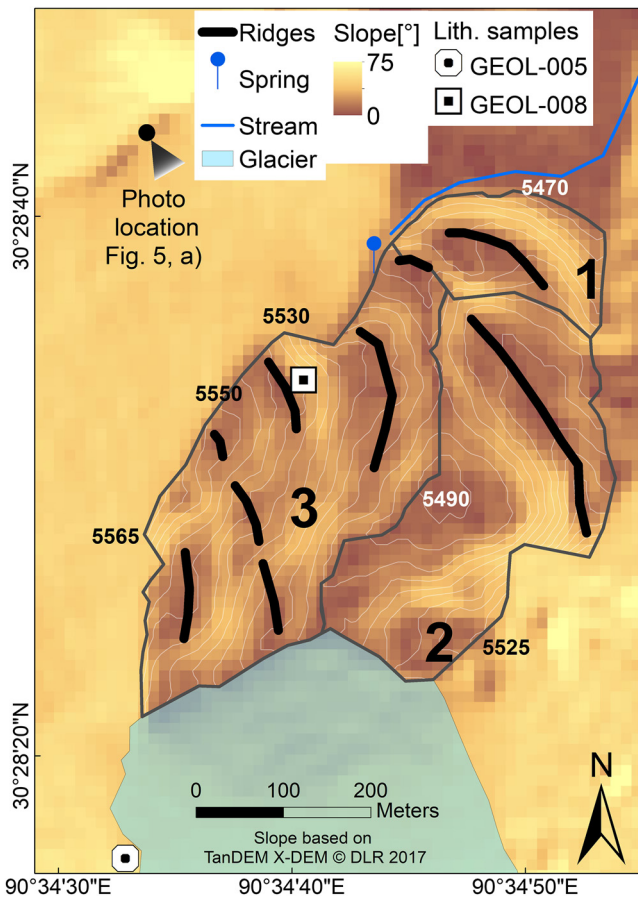


**Figure 4.** (a) Overview map (contour lines in white) of the studied rock glacier including locations and viewing directions of the photograph in Figure 5a. The classification of section 1 (rock glacier front), 2, and 3 is based on the clast analysis (see text).

the central part of Section 2 is occupied by a large depression. Larger slopes and a higher number of ridges characterize the western part (Section 3) of the rock glacier. Here, variations in the slope indicate a sequence of flat and steep areas in the shape of bulges. The contours (5 m distance) imply a constant increase from the deepest to the highest line, parallel to the western slope.

The dominant lithology of the catchment is granodiorite. However, mylonite, a metamorphic rock that forms under strong shear strain along fast ductile fault zones through crystal-plastic deformation, is also present in about one quarter of the catchment area. It appears almost exclusively on the upper mountain flanks in the head of the valley and west of the ice field (Figure 5a). The transition from granodiorite to mylonite, which marks a local fault zone, is visible by an abrupt change in color, from light gray granodiorite to black mylonite.

The difference in color of the mafic (dark) mylonitic clasts and the felsic (bright) granodioritic clasts is due to their inherent mineral composition (Figure 5b). Mylonite shows a greater abundance of mafic porphyroclastic and secondary minerals (~30%–60%), while granodiorites mainly consist of felsic igneous minerals (~95%). The mylonite is a metamorphic rock that forms generally under strong shear strain along fast ductile fault zones through crystal-plastic deformation. It is characterized by significantly smaller overall crystal grain sizes and textural high stress indications, such as dynamic quartz recrystallization, granulation, foliation and augen texture.

The differentiation between the two lithologies is also evident in ternary diagrams quantifying the local clast distribution. The diagrams reveal different clast shapes at the western and eastern part of the rock glacier. The 188 samples in the western part (Section 3; Figure 5c) show a difference in clast type distribution compared to the 187 samples in the eastern part (Section 2; Figure 5d). The western part contains more platy and blocky clasts and fewer elongated clasts, whereas the eastern part is characterized by many blocky clasts and fewer platy or elongated shapes. This is also reflected by the significantly larger average length of the orthogonal axes A and B (Figure 5e).

## 4.2. Subsurface Ice Distribution and Active Layer Thickness

### 4.2.1. ERT and GPR

To investigate the subsurface structure of the rock glacier, five ERT-profiles were collected which indicate a broad range of resistivity values. The first part of tomogram (a) (Figure 6a, dashed line) is located on a plain and vegetation covered valley-floor without any surface-roughness (0–110 m). This area is currently not affected by the studied rock glacier or any other glacial processes. The second part covers the rock glacier front (dashed line, according to Section 1) between 110 and 210 m along the profile. The resistivity values are relatively low, with values <50 kΩm across the first 20 m of depth. A second layer with higher resistivity values (50–100 kΩm) extends through the entire tomogram (a).

A much larger resistivity range from <1 kΩm to 4 MΩm characterizes the ERT tomograms (b–e). A layered structure is visible, which consists of a first, shallow layer with significantly smaller resistivity, and a second, deeper layer with significantly higher resistivity values. The shallow layer is characterized by resistivity values generally below 50 kΩm, and irregular segments with resistivity values of up to 75 kΩm (Figure 6d). The thickness of this layer varies between 2 and 8 m. The suggested layering derived from ERT-data is also observed in the collocated GPR data (Figure 6di vs. 6dii and 6diii). The first layer is characterized by a smaller diffuse reflectivity (Figure 6di) compared to that of the second layer. In the second layer, the higher resistivity values correspond to a higher diffuse reflectivity (Figures 6dii and 6diii).

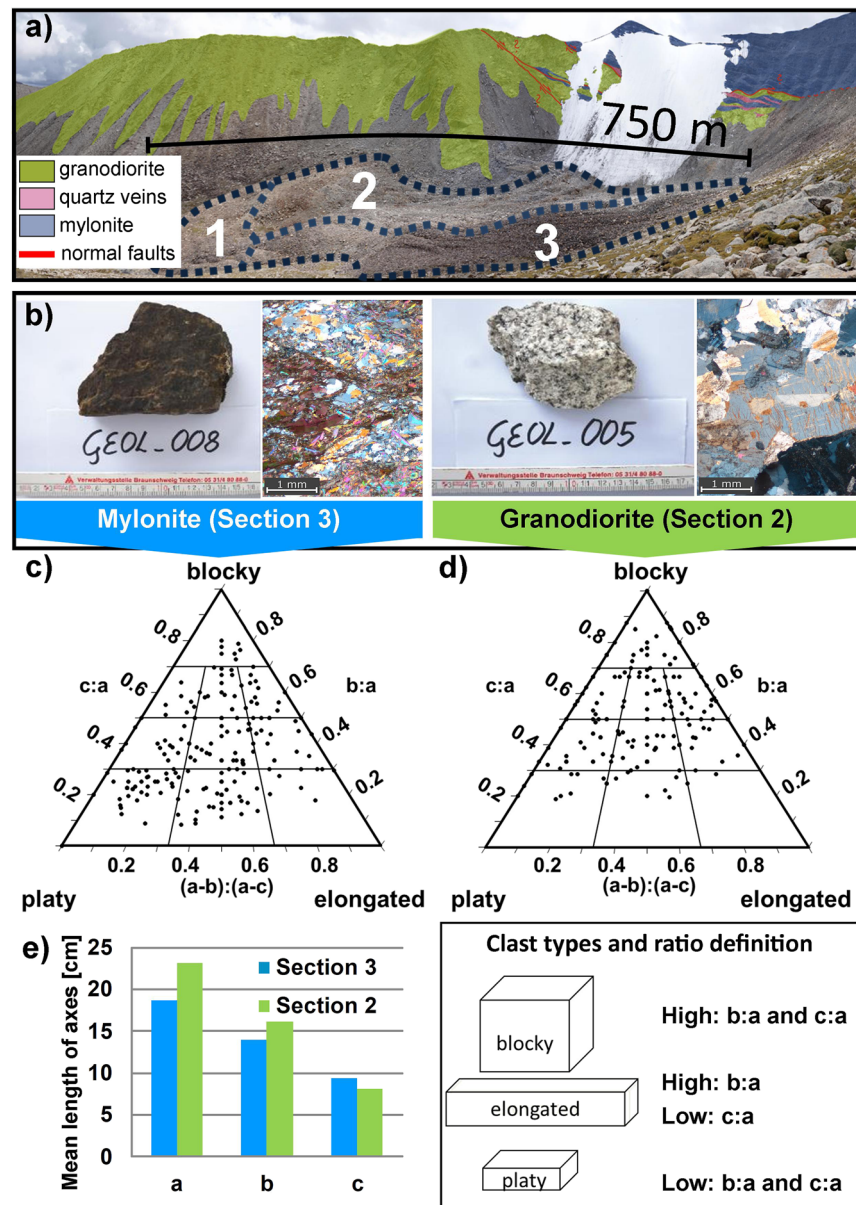


**Figure 5.** (a) Panorama view of the rock glacier including the zonation into 3 sections and the bedrock geology. The red lines indicate the normal fault. (Photo: J. Buckel). (b) Samples and thin sections of mylonite and granodiorite. (c and d) Clast characteristics presented in triangular diagrams according to Benn and Ballantyne (1993) of the granodioritic part (Section 3) and the mylonitic part (Section 2) of the rock glacier: Ternary diagrams represent the clast shapes according to Graham and Midgley (2000). (e) Mean lengths of the three orthogonal clast axes. The legend of clast types and ratio definitions are based on Ballantyne (1982).

The second layer recurs in the ERT tomograms (b–e), which cover a large range of resistivity values (50 kΩm–4 MΩm). The values in tomogram (b) of the eastern rock-glacier part (Section 2) range between 150 kΩm and 2 MΩm between 20 and 85 m along the profile. From 85 to 130 m the resistivity values exceed 2 MΩm. Tomogram (c) on the western part of the rock glacier (Section 3) starts at the lateral slope (0–35 m along the X-axis) and indicates high resistivity values between 150 kΩm and 2 MΩm, too. From 35 to 90 m, the resistivity values slightly decrease before dropping to values <50 kΩm between 90 and 120 m. The second layer of tomogram D includes resistivity values in the same range as tomograms (b and c) (150 kΩm to 2 MΩm). Between 150 and 180 m, the resistivities increase to values higher than 2 MΩm. This zone is approx. 15 m thick and underlies a mapped ridge of the rock glacier. In the same section, the GPR-profile indicates less reflective material compared to the

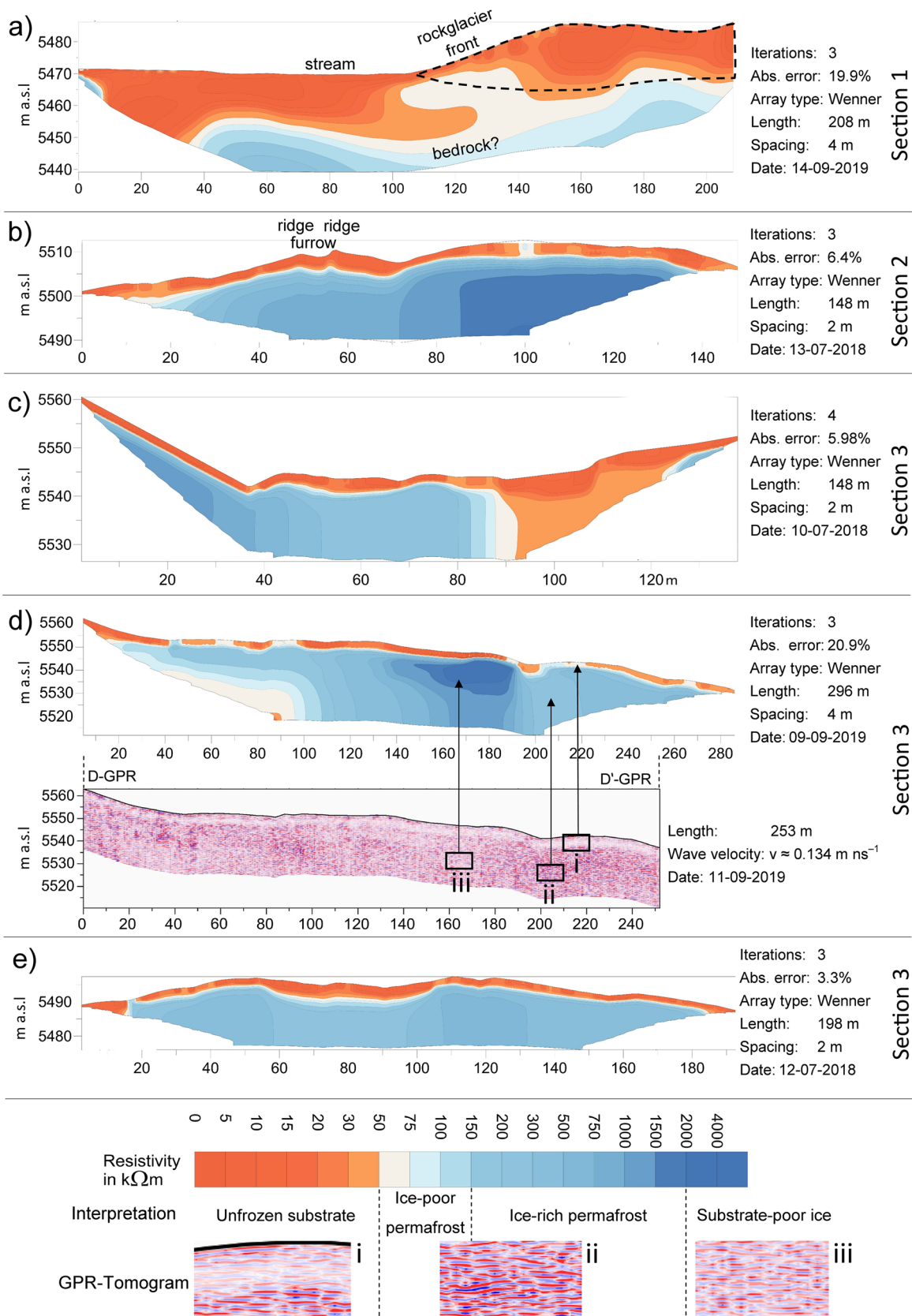
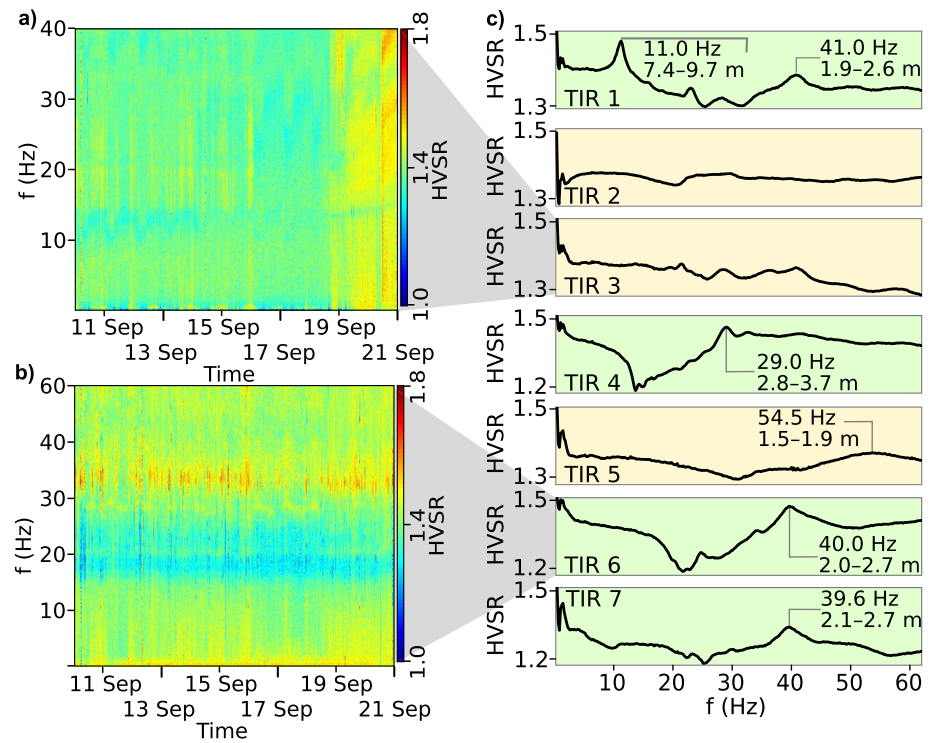


Figure 6.



**Figure 7.** Horizontal-to-vertical spectral ratio (HVSR) analysis results of the seven seismic stations on the rock glacier. The corresponding station location is indicated in Figures 2 and 3. (a) HVSR-value, color-coded as function of time and frequency. Example of a poorly developed time-resolved HVSR series, which is representative for the averaged ratios with yellow background in panel (c). (b) Example of well-developed HVSR series, which is representative for the ratios with green background. (c) HVSR versus frequency for the seven stations, and active layer depth derived from the corresponding spectral peaks.

surrounding area (Figure 6iii). Tomogram (e) in Section 3 underpins the two-layer structure seen in tomogram (b–d) without any significant inhomogeneities.

#### 4.2.2. Active Layer Thickness by Seismic Depth Analysis

Another way to assess the overall thickness of the active layer is to invert the seismic data. The results of the seven seismic stations (location in Figure 2) show two clusters of HVSR phenomena. Stations TIR01, TIR04, TIR06, and TIR07 (Figures 7b and 7c) yield temporally persistent and clear spectral ratio peaks, which in general range between 29 and 41 Hz. Station TIR01 shows a further spectral ratio peak at 11 Hz. Taking the range of possible velocities (325–425 m/s) into account, these spectral ratios translate into resonance layer thicknesses of 1.9–2.6 m for the high frequency peak as well as 7.5–9.7 m for the low frequency peak (TIR01), 2.8–3.7 m (TIR04), 2.0–2.7 m (TIR06) and 2.1–2.7 m (TIR07). In contrast, stations TIR02, TIR03 and TIR05 indicate considerably less pronounced and stable HVSR peaks. Only station TIR05 displays a slight but broad peak around 54.5 Hz, corresponding to a resonance layer thickness of 1.5–1.9 m.

**Figure 6.** Panels (a–e) illustrates the results of the electrical resistivity tomography (ERT)- and ground penetration radar (GPR)-measurements. The dashed line of tomogram A indicates the supposed rock glacier front in Section 1. Profile B is located in the eastern Section 2. Section 3 is represented by profiles (c–e). The GPR-profile (D-GPR—D'-GPR) is located along the ERT-profile (d). The correspondence between GPR reflectivity and ERT resistivity is indicated by three rectangles (i, ii, and iii) and the corresponding arrows.

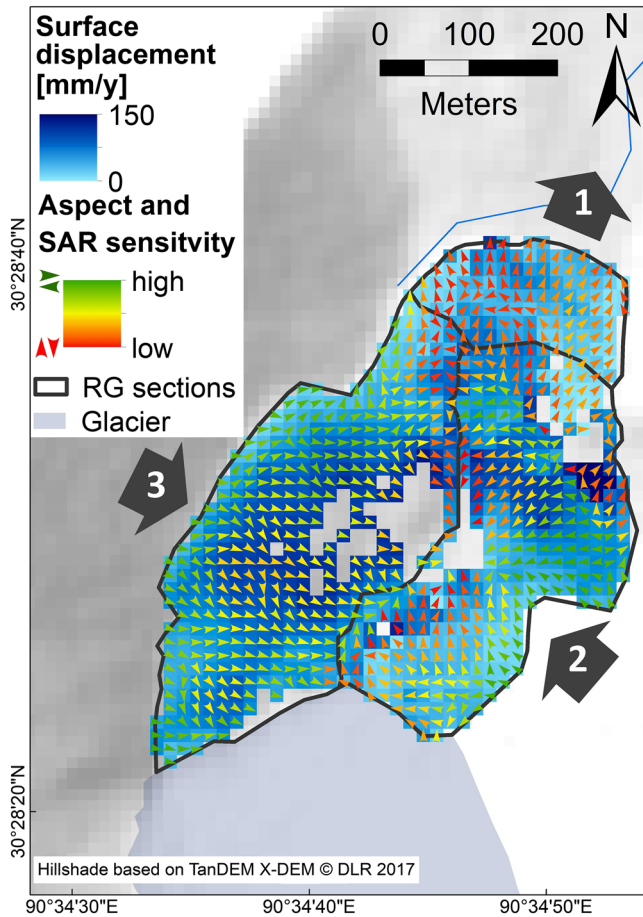


**Figure 8.** Mean annual creeping direction (2015–2018) of the rock glacier's surface and the corresponding SAR sensitivity. Black arrows indicate the dominating creeping direction within the three sections.

### 4.3. Kinematics of the Rock Glacier

#### 4.3.1. InSAR-Time Series Analyses (Long-Term Kinematics)

The long-term kinematics estimated with InSAR SBAS indicate heterogeneous creeping directions based on the combination of the mean flow direction and the surface displacement (Figure 8). This creeping pattern is based on 828 rastercells with a coherence  $>0.3$  while 82 rastercells (9%) are excluded due to a coherence  $<0.3$ . Section 1 clusters a mean flow direction toward north out of the cirque. Sections 2 and 3 creep mainly toward the central depression of the rock glacier. The highest surface displacement rates amount up to 150 mm/y. Three main creeping directions with different mean velocities are observed, which roughly correspond to the zonation into the three sections discussed above (black arrows, Figure 8). The frontal lobe (Section 1) creeps toward the north with the lowest median velocity of 20 mm/yr based on 109 rastercells ( $n^{\text{cell}}$ ). The eastern Section 2 creeps mainly toward a central depression located along the border between Sections 2 and 3 at a velocity of 31 mm/yr ( $n^{\text{cell}} = 335$ ). Section 3 shows surface displacement mainly toward the east with 43 mm/yr ( $n^{\text{cell}} = 384$ ), and toward the central depression. The InSAR sensitivity and therefore the reliability of the creeping pattern is the highest in Sections 2 and 3 due to the east-west creeping direction (Reinosch et al., 2020). The reliability in Section 1 is relatively low due to the north-orientated creeping direction.

#### 4.3.2. Seismic Crack Event Location (Short Term Kinematics)

The STA-LTA picking routine yielded several thousands of initial events, which reduced to 1968 potential crack events after applying the automatic rejection criteria. After manual checks (see Text S2 in Supporting Information S1) we received 304 manually confirmed crack signals during the 11 days survey period. Crack events occurred without obvious temporal clusters during the entire survey period (Figure 9a). However, at the diurnal scale, cracks happened most frequently during night time, peaking at around 8 a.m. in the morning (Figure 9b). Regarding their spatial distribution, there appear to be two outstanding clusters (Figure 9c): at the outer edges of Sections 1 and 2 of the rock glacier (47% of all events) and along the western margin of

the upper part (Section 3) of the rock glacier (53% of all events). When taking into account the location uncertainty and thus grouping the events based on the three sections of the rock glacier with an outer buffer of 20 m, 73 cracks are located in Section 1, 68 cracks in Section 2, and 150 cracks in Section 3.

## 5. Discussion

### 5.1. Morphostructure and Geology of the Rock Glacier

The investigated rock glacier is located in a glacial cirque. The morphology of the rock glaciers is characterized by two longitudinal ridges, which we interpret as former lateral moraines and the front of the rock glacier consisting of moraine deposits in the sense of a push moraine (Barsch, 1977; Dusik et al., 2015). The longest ridge in Section 2 surrounds a central depression at 5,490 m a.s.l. that connects with the headwall on which the remaining ice field is located.

Indicative for a previous glacier and glacial transport is the apparent sorting in the clasts along the ridge which is linked to the sourcing area within the catchment. We identified two distinct lithological units in the catchment, the previously known main unit granodiorite (Kapp et al., 2005; Yu et al., 2019) as well as a metamorphically altered unit of mylonite. The mylonite covers about one quarter of the catchment slopes and potentially extends further into neighboring valleys along a fault. The presence of mylonite at an abrupt contact to the granodioritic unit highlights that tectonic structures such a deep crustal fault zone, in which mylonites form, can control the

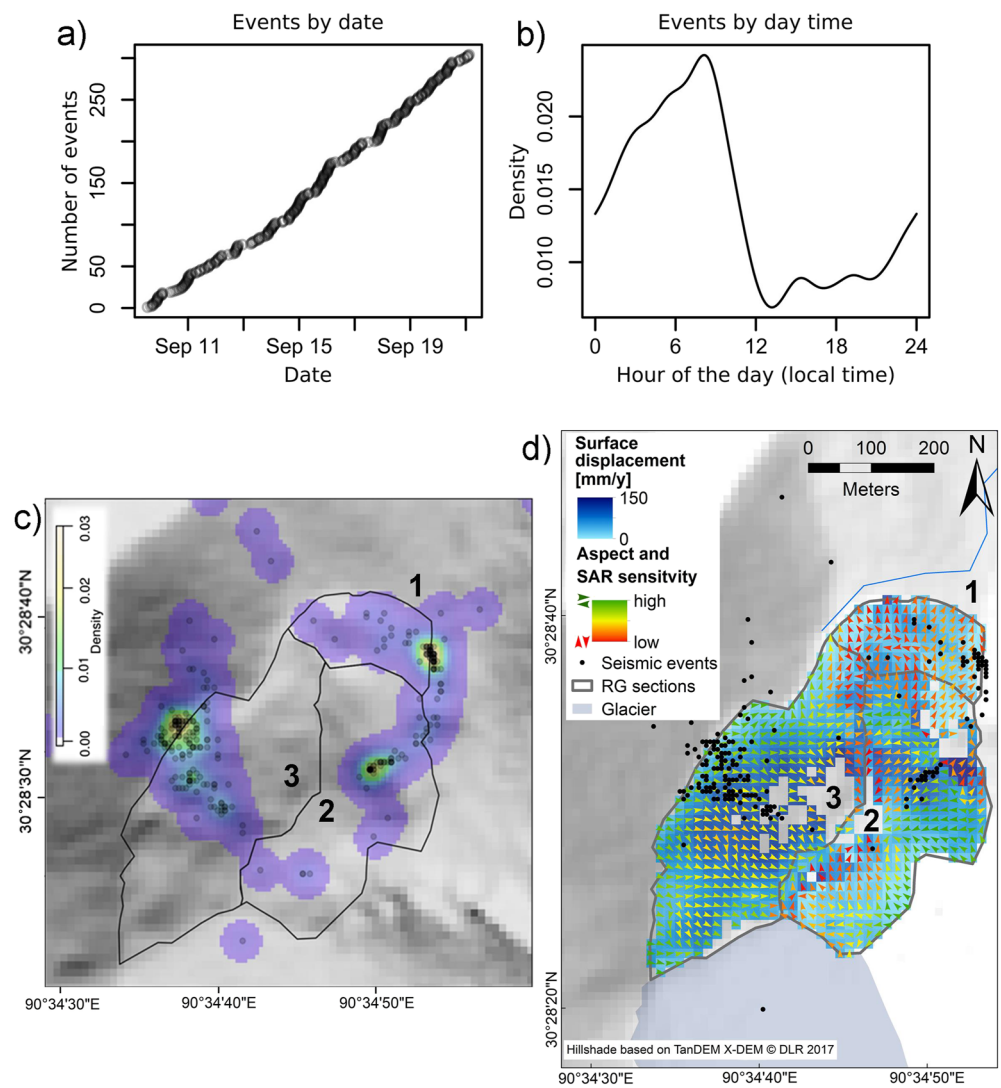


**Figure 9.** Seismic signal characteristics of manually confirmed crack events. (a) Occurrence of events as a function of time throughout the survey period. (b) Occurrence of crack signals at the diurnal scale, shown as kernel density estimate plot. (c) Map showing the crack locations (black dots) and spatial density estimation. (d) Map showing seismic crack locations and creeping behavior derived by InSAR-data.

lithology and especially the debris size and properties. These properties were preserved in the corresponding Section 2 and 3, while Section 1 indicates a stronger clast mixing due to former glacial and recent periglacial processes

Clast size and shape analysis are commonly used to determine the source area, transport path (Jones, Harrison, & Anderson, 2019) or transport distances of supra- and subglacial debris (Benn & Ballantyne, 1994). Usually this methods is applied assuming a single lithological unit (Lukas et al., 2013). In our clast analysis we can clearly see the imprint of the two different lithological units, where the massive granodiorite produces blockier clasts while debris also sourced from the mylonite exhibits platy and elongated shapes as well. The preserved spatial sorting in the ridge in Section 3 points to glacially influenced pathways of the debris (compare Gibson et al., 2017). The periglacial processes have not yet overprint the glacial origin of the sediment sorting. The sorting of clasts is thus preconditioned by the geology and its spatial pattern conditions by past glacial transport processes.

To form a rock glacier, the catchment needs to source enough debris. A previous study in the humid climate of the alps found that large rock glaciers preferentially form in rheological strong lithology, like granitoids (Matsuoka & Ikeda, 2001). The reasoning being that the weatherability is low enough to sustain larger blocks for the cover,

while fine-grained materials for the rock glacier body can easily be sources by weathered material, solifluction or debris flows. Alike this study, the main lithological unit of the catchment is granodiorite, a granitoid. Unlike the study by Matsuoka & Ikeda (2001), the climate in the western Nyainqêntanglha range is semiarid. In a semiarid climate the weathering is mainly facilitated by physical weathering, which can cause a limitation in fine-grained material sources. Especially in Section 3, the provenience of mylonites, which are due to their formation, rheologically weaker and highly fractured, might provide the necessary fine grained material need to store water and ice in the rock glacier body.

## 5.2. Subsurface Ice Content

To assess the interior of the rock glacier and estimate the ice content we applied geophysical methods. The ERT and the GPR provide insights into the rock glacier and material properties along transect perpendicular to the main ridges of the rock glacier. The wide range of resistivity values and the layered structure of the subsurface evident of tomograms (b–e) (Figure 6) is typical for ice-containing rock glaciers (Hauck & Vonder Mùhl, 2003). One exception is tomogram A in Section 1 (Figure 6a). The first layer exhibits resistivity values lower than  $50 \text{ k}\Omega\text{m}$ , which we interpret as unfrozen substrate according to the literature (e.g., Hauck & Kneisel, 2008). A second layer below approximately 20 m shows resistivity values between 50 and  $100 \text{ k}\Omega\text{m}$ . Since core drilling or geophysical methods which provide high resolution at greater depth are not available, we use indirect considerations on the morphology to interpret the layer: Due to the flat terrain in the front of the rock glacier with a complete vegetation cover and absence of any blocky surface roughness, we can exclude a recent influence of the studied rock glacier or any recent glacial processes. Therefore, we assume to detect bedrock with resistivity values between 50 and  $100 \text{ k}\Omega\text{m}$  (similar to unfrozen bedrock shown by Keuschig et al., 2017) underneath an unfrozen sediment layer. The relatively low resistivity within the frontal part (dashed line, Figure 6a) does not show significant contrast and a typical layered structure (active layer and the underlying ice-debris mixture, compare Maurer and Hauck [2007]) of the rock glacier front is missing. We interpret the tomogram (a) in Section 1 as ice-free within the first 20 m depth. Therefore, main parts of the rock glacier front (Section 1) are inactive due to the lack of subsurface ice (Figure 6a) and the resulting missing active layer (Figure 7, TIR 02 + 03). However, the high number of seismic events at the most eastern part of the rock-glacier front indicate an activity of an unknown source. Data from ERT (no measurements in this area) and InSAR (low sensitivity in this area) are not available or not reliable. Therefore, the aggregation of seismic events suggests here brittle deformation and the corresponding existence of subsurface ice in this area (Figure 9d).

Low resistivity values occur in all other tomograms of Section 2 and 3, but mostly in a first shallow layer. We interpret this first shallow layer with a thickness between 2 and 8 m as the active layer, which thaws in the summer month due to raising temperatures and refreezes during the winter month (Barsch, 1996). Since the data was acquired at the end of the summer months, the first layer was typically unfrozen. This hypothesis is consistent with the continuous layer of less intense reflections in the radargram (Figure 6di). The unfrozen substrate of the active layer consists of clasts and air, both characterized by low permittivity. This mixture causes fewer reflections due to missing permittivity contrasts (Berthling & Melvold, 2008). Additionally, the seismic depth analysis based on HVSAR data corresponds well with the depth of the active layer determined by the ERT-/GPR-data. At four locations the depth of the resonance layer is between almost 2 m and about 8 m (Figure 7c), consistent with the transition from low resistivity values ( $<50 \text{ k}\Omega\text{m}$ ) to ice-containing high resistivity values (Figures 6b–6e).

The second layer of tomograms (b–e) (Figure 6) shows generally higher resistivity values. We interpret the values between  $50 \text{ k}\Omega\text{m}$  and  $4 \text{ M}\Omega\text{m}$ , which are typical for rock glaciers, as an ice-containing permafrost body (Dusik et al., 2015; Ikeda, 2006). We classify the resistivity values between  $50 \text{ k}\Omega\text{m}$  and  $150 \text{ k}\Omega\text{m}$  as ice-poor permafrost and the range between  $150 \text{ k}\Omega\text{m}$  and  $2 \text{ M}\Omega\text{m}$  as ice-rich permafrost. These two material types cause a similar pattern in the GPR data, characterized by strong reflections due to a significant amount of ice-interspersed coarser clasts (Figure 6dii).

The zone with especially high resistivity values ( $>2 \text{ M}\Omega\text{m}$ ) in tomogram D occurring under a ridge indicates a massive ice lens. In the GPR-data, the ice lens is characterized by weaker reflections (Figure 6diii), due to smaller permittivity contrasts in the homogeneous medium, as reported by Degenhardt (2009) and Farbrot et al. (2005). Additionally, most seismic events and fastest average displacement rates were recorded in the same zone of highest resistivity values, which suggests the highest subsurface deformation by substrate-poor ice.

Subdivisions into ice-poor and ice-rich permafrost to characterize ice content have been reported in earlier studies (Hauck & Kneisel, 2008; Kenner et al., 2019; Mewes et al., 2017). The exceedingly high resistivity values ( $>2 M\Omega\text{m}$ ) observed here have been interpreted as “temperate glacier ice” ( $10^6$ – $10^8 \Omega\text{m}$ ) by Hauck and Kneisel (2008) or “ground with massive sedimentary ice” ( $150 k\Omega\text{m}$ – $12 M\Omega\text{m}$ ) by Kellerer-Pirklbauer and Kaufmann (2018). We suggest to use a non-genetic term (substrate-poor-ice), which is based on the typical substrate components (rock, water, air, and ice) of a rock glacier (compare Hauck et al. [2008]). The classification allows an interpretation as glacial ice remnants with a recent periglacial characteristic like a typical active layer with a homogeneous thickness. Glacial ice remnants require a superficial, thermal insulation layer based on debris type. The material for the layer could be provided by the coverage of a former debris covered glacier, by remnants of a lateral moraine or by increased paraglacial slope and rockfall activity after glacier retreat (Bolch & Gorbunov, 2014; Dusik et al., 2015; Kellerer-Pirklbauer & Kaufmann, 2018).

To evaluate the volumetric ice content of the rock glacier, a complete delineation of ice-containing permafrost body is required (Halla et al., 2021; Kellerer-Pirklbauer et al., 2017). The lower boundary of the ice-containing permafrost body was not detected by the used methods due to a lack of penetration depth. The increased spacing of the ERT electrodes by 4 m in the second field season did not sufficiently increase the depth of investigation—most probably due to a lack of current strength. The GPR-equipment used a frequency of 100 MHz, which turned out to be too high to achieve larger penetration depths, probably due to scattering caused by large boulders. The fact that no basement was detected means that it must be deeper than the actual depths of investigation. Some internal structures are characterized by very high resistivity values, which additionally prevent deeper penetration of current flow. However, the used methods could identify the ice content and spatial distribution, which provides ground truthing for the remote observations and interpretation of the rock glaciers kinematics.

### 5.3. Rock Glacier Kinematics

In the InSAR displacements we can detect heterogeneous kinematics which suggest different clusters of creeping directions and activity (Figures 9c and 9d). These clusters match the three sections made, based on the morphology and on the internal ice content distribution of the rock glacier. We use the sectioning to distinguish between different activity patterns (Delaloye et al., 2013; Ulrich et al., 2021).

We assume that regions of higher crack activity are indicative of regions with enhanced internal deformation of the rock glacier. If all cracks were just caused by thermal stress (e.g., Polvi et al., 2020; Weber et al., 2018) the distribution of their signals in space would need to be much more homogeneous than visible in our clustered results (Figure 9). The link between crack activity of seismic events and brittle deformation has been demonstrated and justified by physical considerations before (Dietze et al., 2020; Guillemot et al., 2020; Zeckra et al., 2015).

The advantage of InSAR-data is the possibility to identify multiannual surface displacements over a large spatial scale. However, a drawback emerges from the poor InSAR sensitivity in North-South flight directions of the satellite (Reinosch et al., 2020), which unfortunately is the orientation of our catchment. With the seismic network on the rock glacier we could also detect further spatial activity clusters, which can be linked to areas of higher ice content and InSAR.

We find these activity clusters in Section 2 on the longest ridge and more frequent in Section 3 (Figure 9d), which are characterized by substrate-poor ice combined with fastest creeping rates by InSAR-data. Overall, the long- and short-term surface displacement follows the steepest slope toward the central depression.

Additionally, the monitoring of seismic events provides insight into the temporal, diurnal activity patterns. Our data suggests that most seismic events occur at night until early morning (Figure 9b) in the studied late summer period. Seismic crack signals emerge upon brittle deformation and, hence, a net displacement of mass. Ikeda et al. (2008) show that seasonal variations of rock glacier deformation are triggered by numerous temperature changes around the freezing point in combination with water availability. These authors also found that a low winter temperature results in a reduced deformation due to refreezing of pore water. Similarly, Cicoira et al. (2019) concluded that water and external temperature variations control rock glacier dynamics on a seasonal and inter-annual time scale. The present rock glacier lacks a seasonal and perennial kinematical pattern (Buckel et al., 2021). Therefore, if water plays a role for its dynamics, for example, by refreezing, this happens most likely at a diurnal scale.

#### 5.4. Implications for the Rock Glacier Identification, Development, and Exposition Under the Special Climate Setting

Glacially and geologic conditioned, the recent landform still shows typical features of a rock glacier. The superficial features (furrows and ridges, Figure 4), the relatively constant active layer thickness (Figures 6 and 7), the heterogeneous creeping behavior caused by different ice content (Figure 8) and the typical steep front let us classify the recent landform as a debris rock glacier according to Barsch (1996). Ice cliffs and ponds which are typical for debris covered glaciers are absent (compare Sakai et al. [2000]). However, the subsurface ice content of substrate-poor ice could originate from a former glacier, which covers the catchment during the last glacial maximum (J. Yao et al., 2021). Based on its particular characteristics we categorize the studied rock glacier as a transitional landscape feature in a landscape continuum according to Giardino and Vitek (1988). In the nature of a continuum clear borders in a landform development are difficult to identify. The mentioned continuum is also described by Knight et al. (2019) as “glacier to rock glacier transition” or by Anderson et al. (2018) as “glacier—debris covered glacier—rock glacier continuum.” The latter authors pointed out that this continuum ends with an endmember “rock glacier” if the ELA exceeds the headwalls. The ELA for the Qugaqie catchment is given by Bolch et al. (2010) at an elevation around 5,820 m a.s.l. in the year 2009. Ren et al. (2020) calculated an ELA around 6,050 m a.s.l. in 2013–2017 for the entire western Nyainqêntanglha range. The headwall of the studied rock glacier reaches a maximum of nearly 5,800 m a.s.l. (Figure 10a) and therefore lies below the ELA given by Bolch et al. (2010) and Ren et al. (2020). Consequently, we suggest that the studied rock glacier is a typical endmember in the glacier—debris-covered glacier—rock glacier continuum according to Anderson et al. (2018). A small cirque glacier, small avalanche accumulation observed during fieldwork as well as the ice-free rock faces characterizes the north-orientated headwall above the studied rock glacier (compare Figure 5a). This situation is comparable to Anderson et al. (2018, Figure 10): An erosional headwall retreat is observed toward the moisture bringing wind direction (compare the Indian Summer Monsoon in Figure 1a). To extrapolate the concept of Anderson et al. (2018) leads us to the identification of a landscape feature toposéquence which is recurrent in the northern part of the western Nyainqêntanglha range.

The studied debris rock glacier may be structured by the toposéquence along the profile indicated by the yellow line in Figure 1c. The toposéquence along this line, illustrated in Figure 10, consists of (A) debris mantled slopes, (B) cirque glacier, (C) depression, (D) push moraine, and (E) rock glacier front described from south to north. The overall location of debris rock glaciers suggests a systematic occurrence in the northern part western Nyainqêntanglha range (Figure 10). Based on the rock glacier inventory (Buckel & Reinosch, 2021) 48 debris rock glaciers (according to Barsch [1996]) were identified in neighboring valleys. Five exemplary sequences (Figure 10b) are chosen to show debris-rock glaciers as the endmembers according to Anderson et al. (2018). In these cases, a consistent aspect-orientation of the sequence is observed at different locations in the northern part of the western Nyainqêntanglha range (Figure 10b), which is based on the main monsoonal wind-direction from the South (Figure 10c). The topographic barrier divides the mountain range into a southern part and a northern part regarding moisture distribution. The southern part is luvward-facing and oriented toward the moisture bringing ISM. The semiarid northern part is on the leeward-facing side of the monsoon and receives less moisture. This climatic feature is reflected today in a larger glacier area (Figure 1 and Bolch et al., 2010) as well in a greater number and faster kinematics of rock glaciers (Reinosch et al., 2021) on the southern part. The northern part receives less moisture expressed by poorer glaciation and limited sediment supply through weathering and erosion inhibiting a more pronounced rock glacier development. Therefore, the special semiarid climate conditions at the northern part reduce the number and development of rock glaciers. Nevertheless, substantial ice content is available to consider these glacially preconditioned rock glaciers as water resources in the semiarid northern part of the western Nyainqêntanglha range.

## 6. Conclusions

A highly elevated rock glacier at the Tibetan Plateau was analyzed by a complementary, in situ multi-method approach that provides the characteristics (morphostructure, ice content, and kinematics) from diurnal to multianual resolution. The heterogeneous kinematics, as well as sediment and ice composition suggest a sectioning into the rock glacier into three zones including a rather inactive frontal rock glacier lobe. The zones of high ice content correspond to a greater ridge and furrow occurrence which indicates high kinematics compared to other parts of the rock glacier. Ice content varies spatially between ice-poor permafrost to substrate-poor ice except in the main

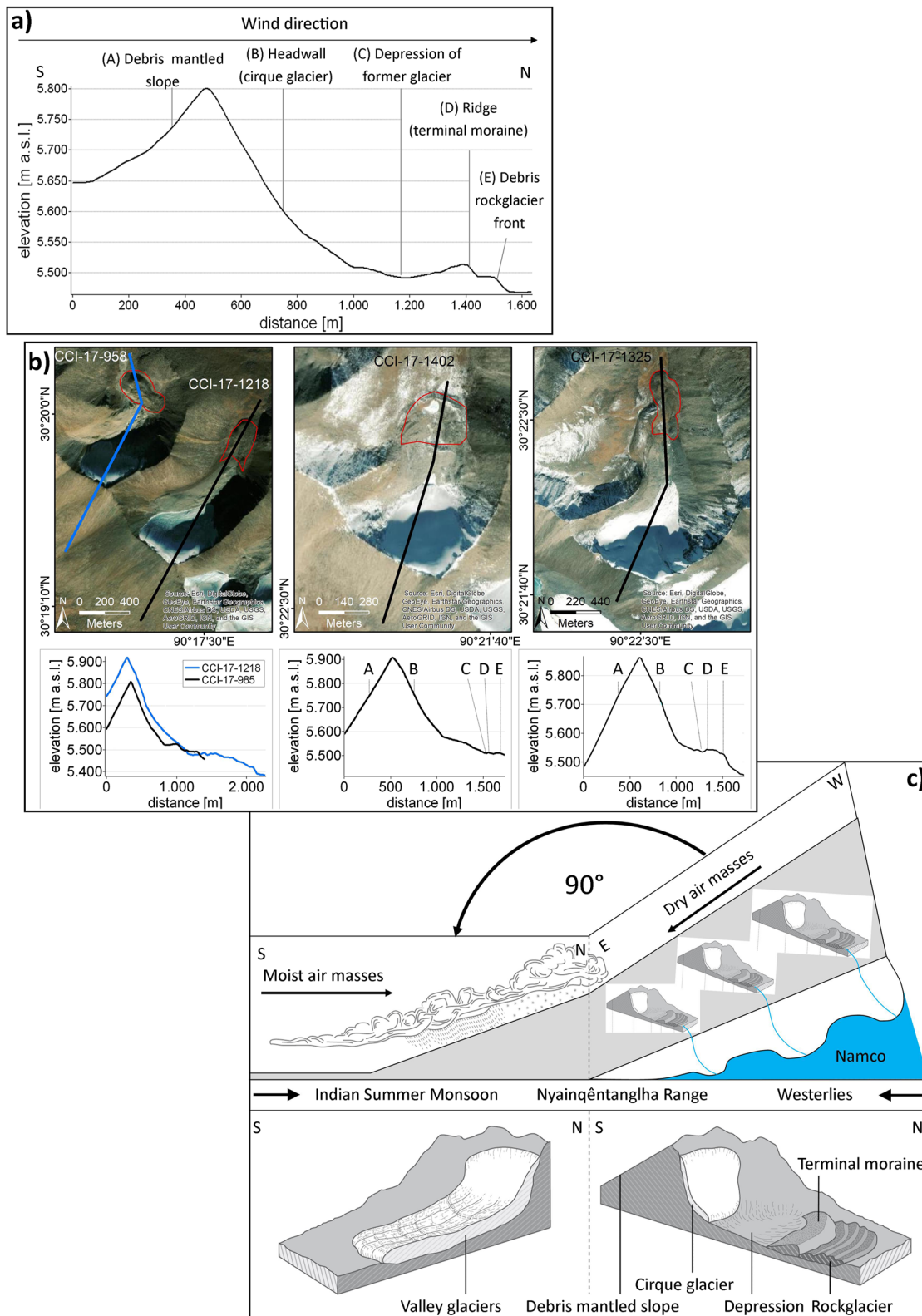


**Figure 10.** (a) Schematic view of the cross section through the studied rock glacier, representing a conceptual toposequence of landscape features based on Profile A (Figure 1c). The end-member is the studied debris-rock glacier. (b) Different rock glaciers from the inventory, which are consistent with the typical climate dependent toposequence, shown by (a). The maps locate the topographic profiles of four exemplary toposequences, which have a similar course. (c) Influence of the regional climate setting on glacier and debris rock glacier distribution over the Nyainqêntanglha Range.

frontal part. A spatially heterogeneous long-termed creeping pattern interpreted from InSAR-data is supported by short-term diurnal and internal seismic event tracking. The locations of highest superficial displacement rates correspond to locations with frequent seismic events. The rock glacier debris consists of two lithological units, mainly granodiorite and mylonite. A debris sorting identified from clast analysis is driven by the preconditioned lithology and maintained during former glaciation.

These characteristics identify the recent landform as a debris rock glacier according to Barsch (1996). The recent debris rock glacier acts as an endmember in a glacier—debris-covered glacier—rock glacier continuum. Typical for these endmembers is the semiarid location behind a topographic barrier (Anderson et al., 2018) like the western Nyainqêntanglha range. Limited availability of moisture and sediment precludes a rock glacier development with huge extents and high ice-content without a glacial imprint like in humid mountain ranges.

This study highlights how regional conditions of geology, topography, and climate influences rock glacier characteristics and development. In large-scaled rock glacier studies that rely on remote sensing methods, the effect of these controls should be considered by measuring data providing ground truth. This becomes especially important when rock glaciers are used as indicators for climate warming or as potential water reservoirs.

## Data Availability Statement

The data obtained by the different methods is available at <https://doi.org/10.5281/zenodo.4751219>.

## Acknowledgments

The authors thank all colleagues who contributed to this study, especially Philipp Maurischat, Felix Nieberding, and Björn Riedel for fruitful discussions and valuable comments before, during and after fieldwork. Special thanks to Chaolu Yi (Institute of Tibetan Plateau Research, Chinese Academy of Sciences), who provided extensive knowledge, photographs, and unpublished material about the glacial history and geomorphology of the Nyainqêntanglha Range. The authors thank the two reviewers, the associated Editor and the Editor for the thoughtful and constructive input. The authors thank Jussi Baade for applying and providing the TanDEM-X data (© DLR), Zhengliang Yu for support in the field, and Guoshuai Zhang and Guangjian Wu for logistical support at the Namors (Nam Co Station for Multisphere Observation and Research, Chinese Academy of Sciences). The authors thank Madhuri Sugand for the intensive review and for the highly valuable suggestions regarding the linguistic and grammatical improvement of the manuscript. The authors thank Ciren Yangzong (Tsering Yangzong) (Urban and Resource Department College Science, Tibet University) for fruitful conversations and discussions about the Tibetan culture and socio-geographical background of the study area. The authors thank the Geophysical Instrument Pool Potsdam GIPP for providing the Digos DataCube<sup>int</sup> data loggers and Geophones. This research is a contribution to the International Research Training Group (GRK 2309/1) “Geo-ecosystems in transition on the Tibetan Plateau (TransTIP)” funded by Deutsche Forschungsgemeinschaft (DFG grant 317513741/GRK 2309). Open access funding enabled and organized by Projekt DEAL.

## References

- Allen, R. (1982). Automatic phase pickers: Their present use and future prospects. *Bulletin of the Seismological Society of America*, 72(6B), S225–S242.
- Anderson, R. S., Anderson, L. S., Armstrong, W. H., Rossi, M. W., & Crump, S. E. (2018). Glaciation of alpine valleys: The glacier–debris-covered glacier–rock glacier continuum. *Geomorphology*, 311, 127–142. <https://doi.org/10.1016/j.geomorph.2018.03.015>
- Anslan, S., Azizi Rad, M., Buckel, J., Echeverria Galindo, P., Kai, J., Kang, W., et al. (2020). Reviews and syntheses: How do abiotic and biotic processes respond to climatic variations in the Nam Co catchment (Tibetan Plateau)? *Biogeosciences*, 17(5), 1261–1279. <https://doi.org/10.5194/bg-17-1261-2020>
- Armijo, R., Tapponnier, P., Mercier, J. L., & Han, T.-L. (1986). Quaternary extension in southern Tibet: Field observations and tectonic implications. *Journal of Geophysical Research*, 91(B14), 13803–13872. <https://doi.org/10.1029/JB091iB14p13803>
- Azócar, G. F., & Brenning, A. (2010). Hydrological and geomorphological significance of rock glaciers in the dry Andes, Chile (27°–33°S). *Permafrost and Periglacial Processes*, 21(1), 42–53. <https://doi.org/10.1002/ppp.669>
- Baddeley, A., Rubak, E., & Turner, R. (2015). *Spatial point patterns: Methodology and applications with R* (1st ed.). Chapman and Hall/CRC.
- Ballantyne, C. K. (1982). Aggregate clast form characteristics of deposits near the margins of four glaciers in the Jotunheimen Massif, Norway. *Norsk Geografisk Tidsskrift*, 36(2), 103–113. <https://doi.org/10.1080/00291958208621960>
- Barsch, D. (1977). Nature and importance of mass-wasting by rock glaciers in alpine permafrost environments. *Earth Surface Processes*, 2(2–3), 231–245. <https://doi.org/10.1002/esp.3290020213>
- Barsch, D. (1996). *Rockglaciers: Indicators for the present and former geocology in high mountain environments*. Springer Science, Springer Berlin Heidelberg.
- Benn, D. I., & Ballantyne, C. K. (1993). The description and representation of particle shape - Short communication. *Earth Surface Processes and Landforms*, 18(4), 665–672. [https://doi.org/10.1016/0006-3207\(72\)90131-0](https://doi.org/10.1016/0006-3207(72)90131-0)
- Benn, D. I., & Ballantyne, C. K. (1994). Reconstructing the transport history of glacial sediments: A new approach based on the co-variance of clast form indices. *Sedimentary Geology*, 91(1–4), 215–227. [https://doi.org/10.1016/0037-0738\(94\)90130-9](https://doi.org/10.1016/0037-0738(94)90130-9)
- Berardino, P., Fornaro, G., Lanari, R., & Sansosti, E. (2002). A new algorithm for surface deformation monitoring based on small baseline differential SAR interferograms. *IEEE Transactions on Geoscience and Remote Sensing*, 40(11), 2375–2383. <https://doi.org/10.1109/TGRS.2002.803792>
- Berthling, I., & Melvold, K. (2008). Ground-penetrating radar. In C. Hauck & C. E. Kneisel (Eds.), *Applied geophysics in periglacial environments* (pp. 81–98). Cambridge University Press.
- Blisniuk, P. M., Hacker, B. R., Glodny, J., Ratschbacher, L., Bi, S., Wu, Z., et al. (2001). Normal faulting in central Tibet since at least 13.5 Myr ago. *Nature*, 412(6847), 628–632. <https://doi.org/10.1038/35088045>
- Blöthe, J. H., Halla, C., Schwalbe, E., Bottegal, E., Trombotto Liaudat, D., & Schrott, L. (2020). Surface velocity fields of active rock glaciers and ice-debris complexes in the Central Andes of Argentina. *Earth Surface Processes and Landforms*, 46(2), 504–522. <https://doi.org/10.1002/esp.5042>
- Bolch, T., & Gorbunov, A. P. (2014). Characteristics and origin of rock glaciers in northern Tien Shan (Kazakhstan/Kyrgyzstan). *Permafrost and Periglacial Processes*, 25(4), 320–332. <https://doi.org/10.1002/ppp.1825>
- Bolch, T., Shea, J. M., Liu, S., Azam, F. M., Gao, Y., Gruber, S., et al. (2019). Status and change of the cryosphere in the extended Hindu Kush Himalaya region. In P. Wester, A. Mishra, A. Mukherji, & A. B. Shrestha (Eds.), *The Hindu Kush Himalaya assessment: Mountains, climate change, sustainability and people* (pp. 209–255). Springer International Publishing. [https://doi.org/10.1007/978-3-319-92288-1\\_7](https://doi.org/10.1007/978-3-319-92288-1_7)
- Bolch, T., Yao, T., Kang, S., Buchroithner, M. F., Scherer, D., Maussion, F., et al. (2010). A glacier inventory for the western Nyainqêntanglha Range and the Nam Co Basin, Tibet, and glacier changes 1976–2009. *The Cryosphere*, 4(3), 419–433. <https://doi.org/10.5194/tc-4-419-2010>
- Buckel, J., & Reinosch, E. (2021). Rockglacier inventory of the western Nyainqêntanglha Range, Tibetan Plateau, Pangaea - Data Publication [Dataset]. Earth and Environmental Science. <https://doi.org/10.1594/PANGAEA.928971>

- Buckel, J., Reinosch, E., Hördt, A., Zhang, F., Riedel, B., Gerke, M., et al. (2021). Insights into a remote cryosphere: A multi method approach to assess permafrost occurrence at the Qugaqie basin, western Nyainqentanglha Range, Tibetan Plateau. *The Cryosphere*, *15*, 149–168. <https://doi.org/10.5194/tc-15-149-2021>
- Cicoira, A., Beutel, J., Faillettaz, J., & Vieli, A. (2019). Water controls the seasonal rhythm of rock glacier flow. *Earth and Planetary Science Letters*, *528*, 115844. <https://doi.org/10.1016/j.epsl.2019.115844>
- Cogley, G., Moelg, N., Frey, H., Guo, W., Raup, B. H., Sakai, A., et al. (2015). *GLIMS glacier database*. National Snow and Ice Data Center. <https://doi.org/10.7265/N5V98602>
- Collier, E., Maussion, F., Nicholson, L. I., Mölg, T., Immerzeel, W. W., & Bush, A. B. G. (2015). Impact of debris cover on glacier ablation and atmosphere-glacier feedbacks in the Karakoram. *The Cryosphere*, *9*(4), 1617–1632. <https://doi.org/10.5194/tc-9-1617-2015>
- Degenhardt, J. J. (2009). Development of tongue-shaped and multilobate rock glaciers in alpine environments – Interpretations from ground penetrating radar surveys. *Geomorphology*, *109*(3–4), 94–107. <https://doi.org/10.1016/j.geomorph.2009.02.020>
- Delaloye, R., Morard, S., Barboux, C., Abbet, D., Gruber, V., Riedo, M., & Gachet, S. (2013). Rapidly moving rock glaciers in Mattertal. In C. Graf (Ed.), *Jahrestagung der Schweizerischen Geomorphologischen Gesellschaft* (p. 164). Eidg. Forschungsanstalt WSL.
- Del Gaudio, V., Muscillo, S., & Wasowski, J. (2014). What we can learn about slope response to earthquakes from ambient noise analysis: An overview. *Engineering Geology*, *182*, 182–200. <https://doi.org/10.1016/j.enggeo.2014.05.010>
- Dietze, M. (2018a). 'eseis' – An R software toolbox for environmental seismology. <https://doi.org/10.5880/GFZ.5.1.2018.001>
- Dietze, M. (2018b). The R package 'eseis'—A software toolbox for environmental seismology. *Earth Surface Dynamics*, *6*(3), 669–686. <https://doi.org/10.5194/esurf-6-669-2018>
- Dietze, M., Krautblatter, M., Illien, L., & Hovius, N. (2020). Seismic constraints on rock damaging related to a failing mountain peak: The Hochvogel, Allgäu. *Earth Surface Processes and Landforms*, *46*(2), 417–429. <https://doi.org/10.1002/esp.5034>
- Dong, G. C., Yi, C. L., & Caffee, M. (2014). <sup>10</sup>Be dating of boulders on moraines from the last glacial period in the Nyainqentanglha mountains, Tibet. *Science China Earth Sciences*, *57*(2), 221–231. <https://doi.org/10.1007/s11430-013-4794-z>
- Duan, A., Wu, G., Liu, Y., Ma, Y., & Zhao, P. (2012). Weather and climate effects of the Tibetan Plateau. *Advances in Atmospheric Sciences*, *29*(5), 978–992. <https://doi.org/10.1007/s00376-012-1220-y>
- Dusik, J.-M., Leopold, M., Heckmann, T., Haas, F., Hilger, L., Morche, D., et al. (2015). Influence of glacier advance on the development of the multipart Riffeltal rock glacier, Central Austrian Alps. *Earth Surface Processes and Landforms*, *40*(7), 965–980. <https://doi.org/10.1002/esp.3695>
- Edwards, M. A., & Ratschbacher, L. (2005). Seismic and aseismic weakening effects in transtension: Field and microstructural observations on the mechanics and architecture of a large fault zone in SE Tibet. *Geological Society, London, Special Publications*, *245*, 109–141. <https://doi.org/10.1144/GSL.SP.2005.245.01.06>
- England, P., & Houseman, G. (1989). Extension during continental convergence, with application to the Tibetan Plateau. *Journal of Geophysical Research*, *94*(B12), 17561–17579. <https://doi.org/10.1029/JB094iB12p17561>
- Farbrøt, H., Isaksen, K., Eiken, T., Ludvig, J., Farbrøt, S., Sollid, A., & Sollid, J. (2005). Composition and internal structures of a rock glacier on the strandflat of western Spitsbergen, Svalbard. *Norsk Geografisk Tidsskrift*, *59*, 139–148. <https://doi.org/10.1080/00291950510020619>
- Fort, M., & van Vliet-Lanoë, B. (2007). Permafrost and periglacial environment of Western Tibet. *Landform Analysis*, *5*, 25–29.
- French, H. M. (2017). *The periglacial environment* (4th ed.). John Wiley & Sons, Ltd.
- Giardino, J. R., & Vitek, J. D. (1988). The significance of rock glaciers in the glacial-periglacial landscape continuum. *Journal of Quaternary Science*, *3*(1), 97–103. <https://doi.org/10.1002/jqs.3390030111>
- Gibson, M. J., Glasser, N. F., Quincey, D. J., Rowan, A. V., & Irvine-Fynn, T. D. (2017). Changes in glacier surface cover on Baltoro glacier, Karakoram, north Pakistan, 2001–2012. *Journal of Maps*, *13*(2), 100–108. <https://doi.org/10.1080/17445647.2016.1264319>
- Graham, D. J., & Midgley, N. G. (2000). Graphical representation of particle shape using triangular diagrams: An excel spreadsheet method. *Earth Surface Processes and Landforms*, *25*(13), 1473–1477. [https://doi.org/10.1002/1096-9837\(200012\)25:13<1473::AID-ESP158>3.0.CO;2-C](https://doi.org/10.1002/1096-9837(200012)25:13<1473::AID-ESP158>3.0.CO;2-C)
- Grebby, S., Orynbasarova, E., Sowter, A., Gee, D., & Athab, A. (2019). Delineating ground deformation over the Tengiz oil field, Kazakhstan, using the Intermittent SBAS (ISBAS) DInSAR algorithm. *International Journal of Applied Earth Observation and Geoinformation*, *81*, 37–46. <https://doi.org/10.1016/j.jag.2019.05.001>
- Guillemot, A., Helmstetter, A., Larose, É., Baillet, L., Garambois, S., Mayoraz, R., & Delaloye, R. (2020). Seismic monitoring in the Gugla rock glacier (Switzerland): Ambient noise correlation, microseismicity and modelling. *Geophysical Journal International*, *221*(3), 1719–1735. <https://doi.org/10.1093/gji/ggaa097>
- Guo, W., Liu, S., Xu, J., Wu, L., Shanguan, D., Yao, X., et al. (2015). The second Chinese glacier inventory: Data, methods and results. *Journal of Glaciology*, *61*(226), 357–372. <https://doi.org/10.3189/2015JG14J209>
- Haerberli, W., Hallet, B., Arenson, L., Elconin, R., Humlum, O., Käab, A., et al. (2006). Permafrost creep and rock glacier dynamics. *Permafrost and Periglacial Processes*, *17*(3), 189–214. <https://doi.org/10.1002/ppp.561>
- Halla, C., Blöthe, J. H., Baldis, C. T., Trombotto, D., Hilbich, C., Hauck, C., & Schrott, L. (2021). Ice content and interannual water storage changes of an active rock glacier in the dry Andes of Argentina. *The Cryosphere*, *15*(2), 1187–1213. <https://doi.org/10.5194/tc-15-1187-2021>
- Harrison, T. M., Copeland, P., Kidd, W. S. F., & Yin, A. N. (1992). Raising Tibet. *Science*, *255*(5052), 1663–1670. <https://doi.org/10.1126/science.255.5052.1663>
- Hauck, C., Bach, M., & Hilbich, C. (2008). A four-phase model to quantify subsurface ice and water content in permafrost regions based on geophysical data sets. In D. L. Kane & K. M. Hinkel (Eds.), *Proceedings of the 9th International Conference on Permafrost* (Vol. 1, pp. 675–680). Institute of Northern Engineering, University of Alaska Fairbank. June 29–July 3, 2008.
- Hauck, C., & Kneisel, C. (2008). *Applied geophysics in periglacial environments*. Cambridge University Press.
- Hauck, C., & Vonder Mühl, D. (2003). Evaluation of geophysical techniques for application in mountain permafrost studies. *Zeitschrift für Geomorphologie*, *132*, 161–190.
- Hausmann, H., Krainer, K., Brückl, E., & Mostler, W. (2007). Internal structure and ice content of Reichenkar rock glacier (Stubai Alps, Austria) assessed by geophysical investigations. *Permafrost and Periglacial Processes*, *18*, 351–367. <https://doi.org/10.1002/ppp.601>
- Hock, R., Rasul, G., Adler, C., Cáceres, B., Gruber, S., Hirabayashi, Y., et al. (2019). High mountain Areas. In H.-O. Pörtner, D. C. Roberts, V. Masson-Delmote, P. Zhai, M. Tignor, E. Poloczanska, et al. (Eds.), *IPCC Special Report on the Ocean and Cryosphere in a Changing Climate* (p. 94). The Intergovernmental Panel on Climate Change (IPCC).
- Humlum, O. (2000). The geomorphic significance of rock glaciers: Estimates of rock glacier debris volumes and headwall recession rates in West Greenland. *Geomorphology*, *35*(1–2), 41–67. [https://doi.org/10.1016/S0169-555X\(00\)00022-2](https://doi.org/10.1016/S0169-555X(00)00022-2)
- Ikeda, A. (2006). Combination of conventional geophysical methods for sounding the composition of rock glaciers in the Swiss Alps. *Permafrost and Periglacial Processes*, *17*, 35–48. <https://doi.org/10.1002/ppp.550>

- Ikeda, A., & Matsuoka, N. (2006). Pebbly versus bouldery rock glaciers: Morphology, structure and processes. *Geomorphology*, 73(3–4), 279–296. <https://doi.org/10.1016/j.geomorph.2005.07.015>
- Ikeda, A., Matsuoka, N., & Kääh, A. (2008). Fast deformation of perennially frozen debris in a warm rock glacier in the Swiss Alps: An effect of liquid water. *Journal of Geophysical Research*, 113(1), 1–12. <https://doi.org/10.1029/2007JF000859>
- Immerzeel, W. W., Lutz, A. F., Andrade, M., Bahl, A., Biemans, H., Bolch, T., et al. (2020). Importance and vulnerability of the world's water towers. *Nature*, 577(7790), 364–369. <https://doi.org/10.1038/s41586-019-1822-y>
- Janke, J. R., & Frauenfelder, R. (2008). The relationship between rock glacier and contributing area parameters in the Front Range of Colorado. *Journal of Quaternary Science*, 32(2), 153–163. <https://doi.org/10.1002/jqs.1133>
- Jarvis, A., Guevara, E., Reuter, H. I., & Nelson, A. D. (2008). *Hole-filled SRTM for the globe: Version 4: Data grid*.
- Jones, D. B., Harrison, S., & Anderson, K. (2019). Mountain glacier-to-rock glacier transition. *Global and Planetary Change*, 181, 102999. <https://doi.org/10.1016/j.gloplacha.2019.102999>
- Jones, D. B., Harrison, S., Anderson, K., & Betts, R. A. (2018). Mountain rock glaciers contain globally significant water stores. *Scientific Reports*, 8(1), 1–10. <https://doi.org/10.1038/s41598-018-21244-w>
- Jones, D. B., Harrison, S., Anderson, K., Selley, H. L., Wood, J. L., & Betts, R. A. (2018). The distribution and hydrological significance of rock glaciers in the Nepalese Himalaya. *Global and Planetary Change*, 160, 123–142. <https://doi.org/10.1016/j.gloplacha.2017.11.005>
- Jones, D. B., Harrison, S., Anderson, K., Shannon, S., & Betts, R. A. (2021). Rock glaciers represent hidden water stores in the Himalaya. *The Science of the Total Environment*, 793, 145368. <https://doi.org/10.1016/j.scitotenv.2021.145368>
- Jones, D. B., Harrison, S., Anderson, K., & Whalley, W. B. (2019). Rock glaciers and mountain hydrology: A review. *Earth-Science Reviews*, 193, 66–90. <https://doi.org/10.1016/j.earscirev.2019.04.001>
- Juliussen, H., & Humlum, O. (2008). Thermal regime of openwork block fields on the mountains Elgåhogna and Sølen, central-eastern Norway. *Permafrost and Periglacial Processes*, 19(1), 1–18. <https://doi.org/10.1002/ppp.607>
- Kääh, A. (2008). Remote sensing of permafrost-related problems and hazards. *Permafrost and Periglacial Processes*, 19(2), 107–136. <https://doi.org/10.1002/ppp>
- Kapp, J. L. D. A., Harrison, T. M., Kapp, P., Grove, M., Lovera, O. M., & Lin, D. (2005). Nyainqentanglha Shan: A window into the tectonic, thermal, and geochemical evolution of the Lhasa block, southern Tibet. *Journal of Geophysical Research*, 110(B8), 1–23. <https://doi.org/10.1029/2004JB003330>
- Karjalainen, O., Luoto, M., Aalto, J., Eitzelmüller, B., Grosse, G., Jones, B., et al. (2020). High potential for loss of permafrost landforms in a changing climate. *Environmental Research Letters*, 15(10), 104065. <https://doi.org/10.1088/1748-9326/abaf5>
- Keil, A., Berking, J., Mügler, I., Schütt, B., Schwalb, A., & Steeb, P. (2010). Hydrological and geomorphological basin and catchment characteristics of Lake Nam Co, South-Central Tibet. *Quaternary International*, 218(1–2), 118–130. <https://doi.org/10.1016/j.quaint.2009.02.022>
- Kellerer-Pirklbauer, A., & Kaufmann, V. (2018). Deglaciation and its impact on permafrost and rock glacier evolution: New insight from two adjacent cirques in Austria. *Science of The Total Environment*, 621, 1397–1414. <https://doi.org/10.1016/j.scitotenv.2017.10.087>
- Kellerer-Pirklbauer, A., Lieb, G. K., & Kaufmann, V. (2017). The Dösen Rock Glacier in Central Austria: A key site for multidisciplinary long-term rock glacier monitoring in the Eastern Alps. *Australian Journal of Earth Sciences*, 110(2). <https://doi.org/10.17738/ajes.2017.0013>
- Kenner, R., Noetzi, J., Hoelzle, M., Raetzo, H., & Phillips, M. (2019). Distinguishing ice-rich and ice-poor permafrost to map ground temperatures and ground ice occurrence in the Swiss Alps. *The Cryosphere*, 13(7), 1925–1941. <https://doi.org/10.5194/tc-13-1925-2019>
- Keuschig, M., Krautblatter, M., Hartmeyer, I., Fuss, C., & Schrott, L. (2017). Automated electrical resistivity tomography testing for early warning in unstable permafrost rock walls around alpine infrastructure. *Permafrost and Periglacial Processes*, 28(7), 158–171. <https://doi.org/10.1002/ppp.1916>
- Kidd, W. S. F., Yusheng, P., Chengfa, C., Coward, M. P., Dewey, J. F., Gansser, A., et al. (1988). Geological mapping of the 1985 Chinese—British Tibetan (Xizang—Qinghai) Plateau Geotraverse route. *Philosophical Transactions of the Royal Society A: Mathematical, Physical and Engineering Sciences*, 327(1594), 287–305. <https://doi.org/10.1098/rsta.1988.0130>
- Kneisel, C., Hauck, C., Fortier, R., & Moorman, B. (2008). Advances in geophysical methods for permafrost investigations. *Permafrost and Periglacial Processes*, 19(2), 157–178. <https://doi.org/10.1002/ppp.616>
- Knight, J. (2019). A new model of rock glacier dynamics. *Geomorphology*, 340, 153–159. <https://doi.org/10.1016/j.geomorph.2019.05.008>
- Knight, J., Harrison, S., & Jones, D. B. (2019). Rock glaciers and the geomorphological evolution of deglaciating mountains. *Geomorphology*, 324, 14–24. <https://doi.org/10.1016/j.geomorph.2018.09.020>
- Krebs, N., Voigtländer, A., Bücker, M., Hördt, A., Schroeckh, R., & Buckel, J. (2020). Pushing the limits of electrical resistivity tomography measurements on a rock glacier at 5500 m a.s.l. on the Tibetan Plateau: Successes and challenges. In *EGU General Assembly 2020, Online, 4–8 May 2020* (pp. EGU2020–2309). Online Conference.
- Lapazaran, J. J., Otero, J., Martín-Español, A., & Navarro, F. J. (2016). On the errors involved in ice-thickness estimates I: Ground-penetrating radar measurement errors. *Journal of Glaciology*, 62(236), 1008–1020. <https://doi.org/10.1017/jog.2016.93>
- Law, R., & Allen, M. B. (2020). Diachronous Tibetan Plateau landscape evolution derived from lava field geomorphology. *Geology*, 48(3), 263–267. <https://doi.org/10.1130/G47196.1>
- Li, B., Yu, Z., Liang, Z., & Acharya, K. (2014). Hydrologic response of a high altitude glacierized basin in the central Tibetan Plateau. *Global and Planetary Change*, 118, 69–84. <https://doi.org/10.1016/j.gloplacha.2014.04.006>
- Li, G., & Lin, H. (2017). Recent decadal glacier mass balances over the Western Nyainqentanglha Mountains and the increase in their melting contribution to Nam Co Lake measured by differential bistatic SAR interferometry. *Global and Planetary Change*, 149, 177–190. <https://doi.org/10.1016/j.gloplacha.2016.12.018>
- Li, J., Sheng, Y., Wu, J., Chen, J., & Zhang, X. (2009). Probability distribution of permafrost along a transportation corridor in the northeastern Qinghai province of China. *Cold Regions Science and Technology*, 59(1), 12–18. <https://doi.org/10.1016/j.coldregions.2009.05.012>
- Loke, M. H., & Barker, R. D. (1995). Least-squares deconvolution of apparent resistivity pseudosections. *Geophysics*, 60(6), 1682–1690. <https://doi.org/10.1190/1.1443900>
- Lukas, S., Benn, D. I., Boston, C. M., Brook, M., Coray, S., Evans, D. J. A., et al. (2013). Clast shape analysis and clast transport paths in glacial environments: A critical review of methods and the role of lithology. *Earth-Science Reviews*, 121, 96–116. <https://doi.org/10.1016/j.earscirev.2013.02.005>
- Matsuoka, N., & Ikeda, A. (2001). Geological control on the distribution and characteristics of talus-derived rock glaciers. *Annual Report of the Institute of Geoscience* (Vol. 27, pp. 11–16). University of Tsukuba.
- Maurer, H., & Hauck, C. (2007). Instruments and methods: Geophysical imaging of alpine rock glaciers. *Journal of Glaciology*, 53(180), 110–120. <https://doi.org/10.3189/172756507781833893>
- Mewes, B., Hilbich, C., Delaloye, R., & Hauck, C. (2017). Resolution capacity of geophysical monitoring regarding permafrost degradation induced by hydrological processes. *The Cryosphere*, 11(6), 2957–2974. <https://doi.org/10.5194/tc-11-2957-2017>

- Millar, C. I., Westfall, R. D., & Delany, D. L. (2013). Thermal and hydrologic attributes of rock glaciers and periglacial talus landforms: Sierra Nevada, California, USA. *Quaternary International*, 310, 169–180. <https://doi.org/10.1016/j.quaint.2012.07.019>
- Molnar, P., & Tapponnier, P. (1978). Active tectonics of Tibet. *Journal of Geophysical Research*, 83(B11), 5361–5375. <https://doi.org/10.1029/JB083iB11p05361>
- Monnier, S., & Kinnard, C. (2015). Reconsidering the glacier to rock glacier transformation problem: New insights from the central Andes of Chile. *Geomorphology*, 238, 47–55. <https://doi.org/10.1016/j.geomorph.2015.02.025>
- Monnier, S., & Kinnard, C. (2017). Pluri-decadal (1955–2014) evolution of glacier-rock glacier transitional landforms in the central Andes of Chile (30–33°S). *Earth Surface Dynamics*, 5(3), 493–509. <https://doi.org/10.5194/esurf-5-493-2017>
- Müller, J., Vieli, A., & Gärtner-Roer, I. (2016). Rock glaciers on the run - understanding rock glacier landform evolution and recent changes from numerical flow modeling. *The Cryosphere*, 10(6), 2865–2886. <https://doi.org/10.5194/tc-10-2865-2016>
- Nogoshi, M., & Igarashi, T. (1971). On the amplitude characteristics of microtremor (Part 2). *Journal of the Seismological Society of Japan*, 2, 26–40. (in Japanese with English abstract).
- Notti, D., Herrera, G., Bianchini, S., Meisina, C., García-Davalillo, J. C., & Zucca, F. (2014). A methodology for improving landslide PSI data analysis. *International Journal of Remote Sensing*, 35(6), 2186–2214. <https://doi.org/10.1080/01431161.2014.889864>
- Otto, J. C., Keuschnig, M., Götz, J., Marbach, M., & Schrott, L. (2012). Detection of mountain permafrost by combining high resolution surface and subsurface information - An example from the Glatzbach catchment, Austrian Alps. *Geografiska Annaler: Series A, Physical Geography*, 94(1), 43–57. <https://doi.org/10.1111/j.1468-0459.2012.00455.x>
- Polvi, L. E., Dietze, M., Lotsari, E., Turowski, J. M., & Lind, L. (2020). Seismic monitoring of a subarctic river: Seasonal variations in hydraulics, sediment transport, and ice dynamics. *Journal of Geophysical Research: Earth Surface*, 125(7), 1–22. <https://doi.org/10.1029/2019JF005333>
- Ran, Y., Li, X., Cheng, G., Zhang, T., Wu, Q., Jin, H., & Jin, R. (2012). Distribution of permafrost in China: An overview of existing permafrost maps. *Permafrost and Periglacial Processes*, 23(4), 322–333. <https://doi.org/10.1002/ppp.1756>
- Ran, Z., & Liu, G. (2018). Rock glaciers in Daxue Shan, south-eastern Tibetan Plateau: An inventory, their distribution, and their environmental controls. *The Cryosphere*, 12(7), 2327–2340. <https://doi.org/10.5194/tc-12-2327-2018>
- Reinosch, E., Buckel, J., Dong, J., Gerke, M., Baade, J., & Riedel, B. (2020). InSAR time series analysis of seasonal surface displacement dynamics on the Tibetan Plateau. *The Cryosphere*, 14, 1633–1650. <https://doi.org/10.5194/tc-2019-262>
- Reinosch, E., Gerke, M., Riedel, B., Schwab, A., Ye, Q., & Buckel, J. (2021). Rock glacier inventory of the western Nyainqêntanglha Range, Tibetan Plateau, supported by InSAR time series and automated classification. *Permafrost and Periglacial Processes*, 32(2), 1–16. <https://doi.org/10.1002/ppp.2117>
- Ren, S., Menenti, M., Jia, L., Zhang, J., Zhang, J., & Li, X. (2020). Glacier mass balance in the Nyainqêntanglha Mountains between 2000 and 2017 retrieved from ZiYuan-3 stereo images and the SRTM DEM. *Remote Sensing*, 12(5), 864. <https://doi.org/10.3390/rs12050864>
- Rowley, T., Giardino, J. R., Granados-Aguilar, R., & Vitek, J. D. (2015). *Periglacial processes and landforms in the critical zone*. Elsevier B.V.
- Sakai, A., Takeuchi, N., Fujita, K., & Nakawo, M. (2000). *Role of supraglacial ponds in the ablation process of a debris-covered glacier in the Nepal Himalayas* (Vol. 265, pp. 119–130). IAHS-AISH Publication.
- Sampson, K. M., & Smith, L. C. (2006). Relative ages of pleistocene moraines discerned from pebble counts: Eastern Sierra Nevada, California. *Physical Geography*, 27(3), 223–235. <https://doi.org/10.2747/0272-3646.27.3.223>
- Schmid, M.-O. O., Baral, P., Gruber, S., Shahi, S., Shrestha, T., Stumm, D., & Wester, P. (2015). Assessment of permafrost distribution maps in the Hindu Kush Himalayan region using rock glaciers mapped in Google Earth. *The Cryosphere*, 9(6), 2089–2099. <https://doi.org/10.5194/tc-9-2089-2015>
- Sowter, A., Bateson, L., Strange, P., Ambrose, K., & Syafiudin, M. F. (2013). DInSAR estimation of land motion using intermittent coherence with application to the South Derbyshire and Leicestershire coalfields. *Remote Sensing Letters*, 4(10), 979–987. <https://doi.org/10.1080/2150704X.2013.823673>
- Strozzi, T., Caduff, R., Jones, N., Barboux, C. C., Delaloye, R., Bodin, X., et al. (2020). Monitoring rock glacier kinematics with satellite synthetic aperture radar. *Remote Sensing*, 12(3), 559. <https://doi.org/10.3390/rs12030559>
- Sun, J., Zhou, T., Liu, M., Chen, Y., Shang, H., Zhu, L., et al. (2018). Linkages of the dynamics of glaciers and lakes with the climate elements over the Tibetan Plateau. *Earth-Science Reviews*, 185, 308–324. <https://doi.org/10.1016/j.earscirev.2018.06.012>
- Taylor, M., Yin, A., Ryerson, F. J., Kapp, P., & Ding, L. (2003). Conjugate strike-slip faulting along the Bangong-Nujiang suture zone accommodates coeval east-west extension and north-south shortening in the interior of the Tibetan Plateau. *Tectonics*, 22(4). <https://doi.org/10.1029/2002TC001361>
- Ulrich, V., Williams, J. G., Zahs, V., Anders, K., Hecht, S., & Höfle, B. (2021). Measurement of rock glacier surface change over different timescales using terrestrial laser scanning point clouds. *Earth Surface Dynamics*, 9(1), 19–28. <https://doi.org/10.5194/esurf-9-19-2021>
- Villarroel, C. D., Beliveau, G. T., Forte, A. P., Monserrat, O., & Morvillo, M. (2018). DInSAR for a regional inventory of active rock glaciers in the Dry Andes Mountains of Argentina and Chile with Sentinel-1 data. *Remote Sensing*, 10(10), 1–21. <https://doi.org/10.3390/rs10101588>
- Von der Mühl, D., Hauck, C., & Gubler, H. (2002). Mapping of mountain permafrost using geophysical methods. *Progress in Physical Geography*, 26(4), 643–660. <https://doi.org/10.1191/0309133302pp356ra>
- Walter, F., Burtin, A., McArdell, B. W., Hovius, N., Weder, B., & Turowski, J. M. (2017). Testing seismic amplitude source location for fast debris-flow detection at Illgraben, Switzerland. *Natural Hazards and Earth System Sciences*, 17(6), 939–955. <https://doi.org/10.5194/nhess-17-939-2017>
- Wang, B., Ma, Y., Ma, W., Su, B., & Dong, X. (2019). Evaluation of ten methods for estimating evaporation in a small high-elevation lake on the Tibetan Plateau. *Theoretical and Applied Climatology*, 136(3), 1033–1045. <https://doi.org/10.1007/s00704-018-2539-9>
- Washburn, A. L. (1980). *Geocryology: A survey of periglacial processes and environments*. Wiley.
- Weber, S., Fäh, D., Beutel, J., Failletaz, J., Gruber, S., & Vieli, A. (2018). Ambient seismic vibrations in steep bedrock permafrost used to infer variations of ice-fill in fractures. *Earth and Planetary Science Letters*, 501, 119–127. <https://doi.org/10.1016/j.epsl.2018.08.042>
- Winsor, K., Swanger, K. M., Babcock, E. L., Dickson, J. L., Valletta, R. D., & Schmidt, D. F. (2020). Origin, structure and geochemistry of a rock glacier near Don Juan Pond, Wright Valley, Antarctica. *Antarctic Science*, 32(4), 273–287. <https://doi.org/10.1017/S0954102020000139>
- Wolman, M. G. (1954). A method of sampling coarse river-bed material. *Eos, Transactions American Geophysical Union*, 35(6), 951–956. <https://doi.org/10.1029/TR035i006p00951>
- Yao, J., Chao-lu, Y., Dandan, X., & Nan, Y. (2021). Reconstruction of Palaeoglacier in the Qugaqie valley in Nyainqêntanglha Range. In *IOP Conference Series: Earth and Environmental Science. 2nd International Conference on Geology, Resources Exploration and Development* (Vol. 671). IOP Publishing.
- Yao, T., Masson-Delmotte, V., Gao, J., Yu, W., Yang, X., Risi, C., et al. (2013). A review of climatic controls on  $\delta^{18}\text{O}$  in precipitation over the Tibetan Plateau: Observations and simulations. *Review of Geophysics*, 51(4), 525–548. <https://doi.org/10.1002/rog.20023>

- Yao, T., Thompson, L., Yang, W., Yu, W., Gao, Y., Guo, X., et al. (2012). Different glacier status with atmospheric circulations in Tibetan Plateau and surroundings. *Nature Climate Change*, 2(9), 663–667. <https://doi.org/10.1038/nclimate1580>
- Yatagai, A., & Yasunari, T. (1998). Variation of summer water vapor transport related to precipitation over and around the arid region in the interior of the Eurasian continent. *Journal of the Meteorological Society of Japan. Ser. II*, 76(5), 799–815. [https://doi.org/10.2151/jmsj1965.76.5\\_799](https://doi.org/10.2151/jmsj1965.76.5_799)
- Yin, A., & Harrison, T. M. (2000). Geologic evolution of the Himalayan-Tibetan orogen. *Annual Review of Earth and Planetary Sciences*, 28(1), 211–280. <https://doi.org/10.1146/annurev.earth.28.1.211>
- Yin, A., Kapp, P. A., Murphy, M. A., Manning, C. E., Harrison, T. M., Grove, M., et al. (1999). Significant late Neogene east-west extension in northern Tibet. *Geology*, 27(9), 787–790. [https://doi.org/10.1130/0091-7613\(1999\)027<0787:SLNEWE>2.3.CO;2](https://doi.org/10.1130/0091-7613(1999)027<0787:SLNEWE>2.3.CO;2)
- Yu, Z., Wu, G., Keys, L., Li, F., Yan, N., Qu, D., & Liu, X. (2019). Seasonal variation of chemical weathering and its controlling factors in two alpine catchments, Nam Co basin, central Tibetan Plateau. *Journal of Hydrology*, 576, 381–395. <https://doi.org/10.1016/J.JHYDROL.2019.06.042>
- Zeckra, M., Hovius, N., Burtin, A., & Hammer, C. (2015). Automated detection and classification of rockfall induced seismic signals with hidden-Markov-models. In *AGU Fall Meeting Abstracts* (Vol. 2015, pp. NH34A-04).
- Zou, D., Zhao, L., Sheng, Y., Chen, J., Hu, G., Wu, T., et al. (2017). A new map of permafrost distribution on the Tibetan Plateau. *The Cryosphere*, 11(6), 2527–2542. <https://doi.org/10.5194/tc-11-2527-2017>